JGR Solid Earth

RESEARCH ARTICLE
10.1029/2019JB018597

Nearly Magnitude-Invariant Stress Drops in Simulated Crack-Like Earthquake Sequences on Rate-and-State Faults with Thermal Pressurization of Pore Fluids

Stephen M. Perry[1], Valère Lambert[1], and Nadia Lapusta[1,2]

[1]Seismological Laboratory, California Institute of Technology, Pasadena, CA, USA, [2]Mechanical and Civil Engineering, California Institute of Technology, Pasadena, CA, USA

Key Points:

- Thermal pressurization (TP) results in continuous weakening and increasing breakdown energy with slip
- TP allows larger ruptures to propagate into lower prestress regions, leading to magnitude-invariant stress drops
- Stress drops for large events are impacted by the properties of the arresting velocity-strengthening regions into which they propagate

Correspondence to:
V. Lambert,
vlambert@caltech.edu

Citation:
Perry, S. M., Lambert, V., & Lapusta, N. (2020). Nearly magnitude-invariant stress drops in simulated crack-like earthquake sequences on rate-and-state faults with thermal pressurization of pore fluids. *Journal of Geophysical Research: Solid Earth*, *125*, e2019JB018597. https://doi.org/10.1029/2019JB018597

Received 3 SEP 2019
Accepted 28 FEB 2020
Accepted article online 4 MAR 2020
Corrected 19 MAY 2020

This article was corrected on 19 MAY 2020. See the end of the full text for details.

©2020. The Authors.
This is an open access article under the terms of the Creative Commons Attribution License, which permits use, distribution and reproduction in any medium, provided the original work is properly cited.

Abstract Stress drops, inferred to be magnitude-invariant, are a key characteristic used to describe natural earthquakes. Theoretical studies and laboratory experiments indicate that enhanced dynamic weakening, such as thermal pressurization of pore fluids, may be present on natural faults. At first glance, magnitude invariance of stress drops and enhanced dynamic weakening seem incompatible since larger events may experience greater weakening and should thus have lower final stresses and higher stress drops. We hypothesize that enhanced dynamic weakening can be reconciled with magnitude-invariant stress drops due to larger events having lower average prestress when compared to smaller events. We conduct numerical simulations of long-term earthquake sequences in fault models with rate-and-state friction and thermal pressurization, and in the parameter regime that results mostly in crack-like ruptures, we find that such models can explain both the observationally inferred stress drop invariance and increasing breakdown energy with event magnitude. Smaller events indeed have larger average initial stresses than medium-sized events, and we find nearly constant stress drops for events spanning up to two orders of magnitude in average slip, comparable to approximately six orders of magnitude in seismic moment. Segment-spanning events have more complex behavior, which depends on the properties of the arresting velocity-strengthening region at the edges of the faults.

1. Introduction

Stress drops and breakdown energy are important descriptors of natural earthquakes. Stress drops characterize the average change in stress state from before to after the dynamic event (Kanamori & Anderson, 1975; Knopoff, 1958; Kostrov, 1974). The stress drop distribution varies along the fault and can be averaged in several different ways in order to produce a single, representative value for an event (Section 3). There is a fair amount of scatter in the inferred average values of stress drops of natural earthquakes, from about 0.1 MPa up to values around 100 MPa (Baltay et al., 2011; Kanamori & Brodsky, 2004). However, the inferred values of stress drop are magnitude-invariant; most events have stress drops that fall between 1 MPa and 10 MPa, and this trend has been observed for events ranging nine orders of magnitude in seismic moment (Abercrombie & Rice, 2005; Allmann & Shearer, 2009; Cocco et al., 2016; Ide & Beroza, 2001). The generality of the inferred magnitude invariance of stress drops is still a topic of ongoing research, with some observations indicating that some individual earthquake sequences may exhibit mildly increasing trends in stress drop with increasing moment (e.g., Cocco et al., 2016; Viesca & Garagash, 2015). The interpretation and reliability of the stress drops estimates have been actively studied recently, with indications that the current standard methods of estimating stress drops can introduce some significant discrepancies between the actual and inferred stress drops (e.g., Kaneko & Shearer, 2014, 2015; Lin & Lapusta, 2018; McGuire & Kaneko, 2018; Noda et al., 2013). However, there are no indications at present that the overall nearly magnitude-invariant trend should be questioned.

Breakdown energy, a quantity analogous to fracture energy from singular and cohesive zone models of fracture mechanics, is meant to capture the energy consumed near the rupture tip that controls the dynamics of the rupture front (Cocco et al., 2004; Palmer et al., 1973; Rice, 1980). Breakdown energy is a part of the overall energy budget of a seismic event, with the total strain energy released (ΔW) typically divided into the breakdown energy G, radiated energy E_R, and other dissipation E_D (Kanamori & Rivera, 2013). It is a more straightforward concept for shear stress versus slip behavior that follows slip weakening during dynamic

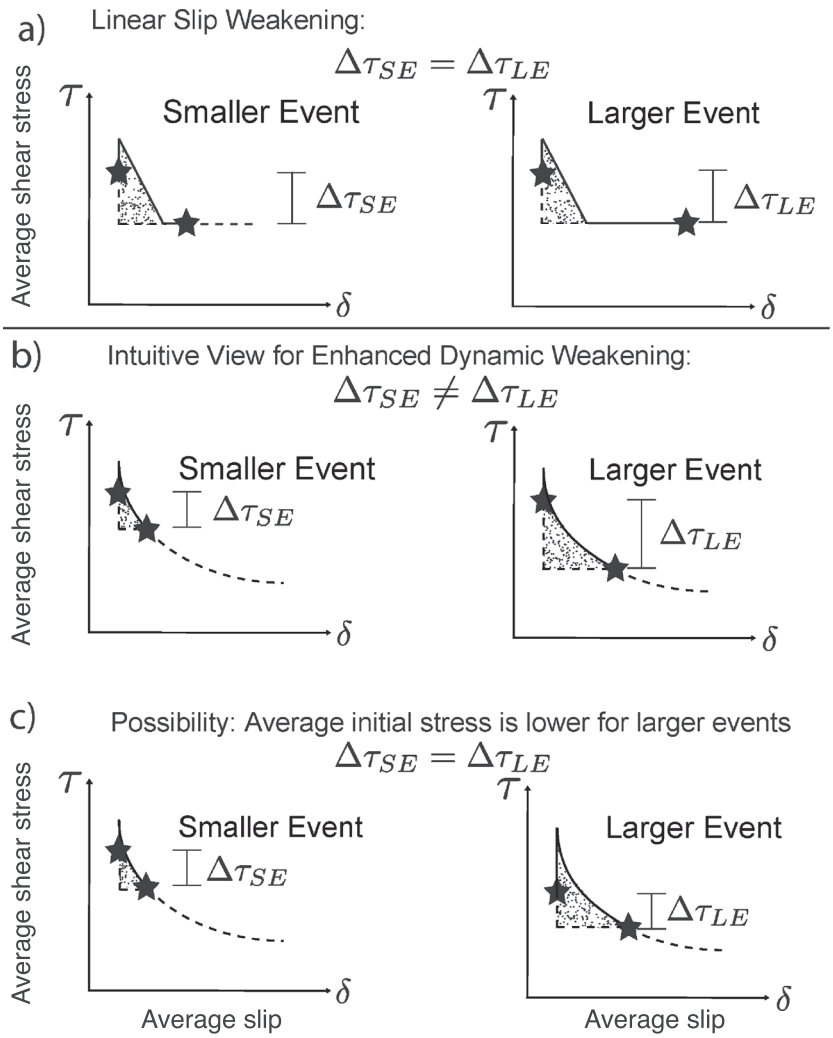

Figure 1. Stress drop and breakdown energy implications for linear slip-weakening and rate-and-state friction with additional dynamic weakening. (a) In linear slip-weakening laws, smaller and larger events weaken to the same dynamic levels of shear resistance over the same slip. This leads to the same breakdown energies (dotted regions) and similar stress drop (marked with stars). (b) If smaller and larger events both nucleate at the same levels of prestress, and larger events weaken more than small events, one expects both larger breakdown energies and larger stress drops for larger events. (c) However, if dynamic weakening allows larger events to propagate into areas of lower stress, then the average prestress of these events may be lower than for smaller events. In this case, breakdown energies still increase with event size, but stress drops may be magnitude-invariant.

rupture (Kanamori & Heaton, 2013; Kanamori & Brodsky, 2004; Rice, 2000). It is calculated by taking the area underneath the stress-slip curve for a single event from initiation to the lowest dynamic level of stress and then subtracting off the frictional energy dissipation (Figure 1 and Section 3). Breakdown energy is inferred to increase with the event size in natural earthquakes (Abercrombie & Rice, 2005; Rice, 2006; Viesca & Garagash, 2015).

It is clear that during dynamic rupture, the fault shear resistance overall decreases, resulting in a stress drop. The exact nature of this evolution is currently an active area of research. Slip-weakening models, where the shear stress decrease depends on the slip accumulated during the event, are commonly used (Ida, 1972; Palmer et al., 1973). Linear slip weakening (LSW) is a simplified model where the shear resistance decreases linearly with slip until it reaches a constant dynamic level (Section 4.1).

Significant insights into the physics of shear resistance during earthquakes have been obtained from the laboratory, showing much richer behavior. At slip rates between 10^{-9} and 10^{-3} m/s, laboratory findings are

well described by the so-called rate-and-state friction laws (Dieterich, 2015, and references therein). Studies using rate-and-state models have successfully reproduced a number of earthquake source observations, including the decay of aftershocks (Dieterich, 1994), sequences of earthquakes on an actual fault segment (Barbot et al., 2012), and repeating earthquakes (Chen & Lapusta, 2009).

At the same time, many experiments and theoretical studies have shown that enhanced dynamic weakening can be a dominating effect during earthquakes (Di Toro et al., 2011). This type of weakening can be caused by several different mechanisms, many of them due to shear heating. Thermal pressurization may be caused by the shear heating of pore fluids during slip (Andrews, 2002; Rice, 2006; Sibson, 1973); if the pore fluid is heated quickly enough and not allowed to diffuse away, it pressurizes and relieves normal stress on the fault. Flash heating is another shear-heating effect of rapid weakening due to microcontacts between the two sides of the fault melting at small scales and rapidly decreasing the effective friction coefficient (Goldsby & Tullis, 2011; Passelégue et al., 2014; Rice, 1999). Other weakening mechanisms can act in the shear zone, including the thermal decomposition of rocks (Han et al., 2007; Sulem & Famin, 2009), macroscopic melting (Goldsby & Tullis, 2002; Di Toro et al., 2004, 2011), elastohydrolubrication (Brodsky & Kanamori, 2001), and silica gel formation (Brodsky & Kanamori, 2001; Di Toro et al., 2004; Goldsby & Tullis, 2002). Considerations of heat production during dynamic rupture are a substantial constraint for potential fault models as field studies rarely suggest the presence of melt and show no correlation between faulting and heat flow signatures (Lachenbruch & Sass, 1980; Sibson, 1975).

Several numerical studies used these enhanced dynamic weakening effects to explain some observations for natural earthquakes. Thermal pressurization of pore fluids can explain the inferred increase in breakdown energy with the increasing event size (Rice, 2006; Viesca & Garagash, 2015); this has been shown using simplified theoretical arguments. Models with dynamic weakening have been successful in producing fault operation at low overall prestress and low heat production (Noda et al., 2009; Rice, 2006) as supported by several observations (Brune et al., 1969; Hickman & Zoback, 2004; Williams et al., 2004; Zoback et al., 1987).

However, it is not clear whether enhanced dynamic weakening is consistent with magnitude-invariant stress drops. In the following intuitive scenario, they are not. Let us assume that smaller and larger events nucleate at nearly the same level of average prestress. The smaller event has less slip and thus weakens a smaller amount. This results in a smaller breakdown energy (the dotted region) and a higher final stress. The larger event weakens more and has a larger breakdown energy and lower final stress. In this scenario, larger events would have systematically larger stress drops and larger breakdown energy (Figure 1b). However, this intuitive scenario may be incorrect, due to the following hypothesis which is illustrated and supported by the simulations in this work. Both smaller and larger events would *nucleate* at locations with relatively high prestress, matching the quasi-static frictional strength. But we must consider the average initial stress of all points involved in the rupture, not just those involved in nucleation. Larger events would have larger slips and hence dynamically weaken more and may be able to propagate over areas of much less favorable (lower) prestress conditions. This means that the initial stress averaged over the entire rupture area may be lower for larger events than that for smaller events. Overall, larger events would dynamically weaken more and potentially arrest at a lower average final stress, but they would also have occurred with lower average initial stress. Thus, the average stress drop can be similar for smaller and larger events (Figure 1c). However, the observed increase of the breakdown energy with event size is still preserved.

Here, we use fully dynamic simulations of earthquake sequences on rate-and-state faults to investigate this hypothesis and study if enhanced dynamic weakening can indeed be compatible with magnitude-invariant stress drops while also maintaining increasing breakdown energy with increasing event size. Different dynamic weakening mechanisms produce different weakening behaviors, but here we focus on thermal pressurization as a representative dynamic weakening mechanism that can lead to continuous fault weakening with earthquake-source slip. We consider the simplest scenario that allows us to explore this hypothesis, that of a seismogenic fault segment with uniform properties of quasi-static fault strength. For heterogeneous faults, the argument should still hold, since larger ruptures with larger slip and hence more pronounced weakening should be able to propagate over larger areas of locally unfavorable prestress, as compared to smaller ruptures, potentially still resulting in nearly magnitude-invariant stress drops, but with some scatter due to heterogeneity. Such scenarios will be investigated in future work.

We indeed find that the hypothesis of lower average initial stress before larger events holds for a wide range of events in our simulations that arrest within the seismogenic region, resulting in nearly magnitude-invariant

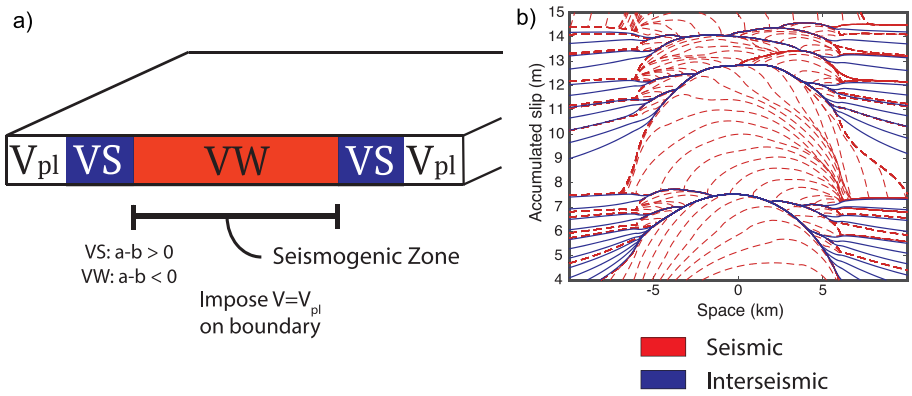

Figure 2. (a) Model setup for our simulations. The fault is composed of a velocity-weakening (VW) seismogenic section surrounded by two velocity-strengthening (VS) patches. Outside of these regions, relative sliding with the plate rate is prescribed. (b) A portion (15 events) of a simulation with the standard rate-and-state friction ($L = 250$ μm) is plotted showing accumulated slip along the fault through time. Seismic events are illustrated by red dashed lines plotted every 0.1 s when slip rate V exceeds 0.1 m/s. Interseismic slip is plotted in solid blue lines every 10 years.

stress drops, at least for the range of parameters considered in this work that results in mostly crack-like ruptures. Our fully dynamic simulations also confirm the increase in breakdown energy with the event size consistent with observations. For seismogenic-region-spanning events, we find that the properties of the velocity-strengthening areas can have a profound impact on the stress drop. Models with large values of velocity strengthening do not allow ruptures to propagate much into the velocity-strengthening region, thus leading to higher stress drops, whereas models with smaller values of velocity strengthening allow farther propagation and thus lower stress drops.

For completeness, we start by investigating faults without enhanced dynamic weakening, with the Dieterich-Ruina rate-and-state friction only. Consistent with related findings of prior studies, we find that the stress drops are also magnitude-independent, but so is the breakdown energy. This is because Dieterich-Ruina rate-and-state friction resembles linear slip-weakening during dynamic rupture (Cocco & Bizzarri, 2002; Lapusta & Liu, 2009), which has prescribed and process-independent dynamic resistance and breakdown energy.

We also use our modeling to examine the accuracy of seismically estimated breakdown energies G_{SE}, by comparing the values computed directly from the on-fault variables with inferred values G_{SE} computed indirectly from seismically available observations.

Here we follow the assumption that most of the breakdown energy occurs on the shearing surface (e.g., Rice, 2006; Viesca & Garagash, 2015). While it is clear that some energy is dissipated in off-fault damage (Andrews, 2005; Poliakov et al., 2002), especially on rough, non-planar faults (Dieterich & Smith, 2009; Dunham et al., 2011), those amounts may be negligible compared to seismic estimates of breakdown energy, at least for relatively planar mature faults. The relative importance of the off-fault and on-fault dissipation during dynamic rupture is an important topic of ongoing studies which is beyond the scope of this work.

2. Fault Model Formulation

Our simulations are conducted following the methodological developments of Lapusta et al. (2000) and Noda and Lapusta (2010). In order to study long sequences of seismic events in simulations with enhanced dynamic weakening, we consider a mode III, two-dimensional (2-D) model with a one-dimensional (1-D) fault embedded into a 2-D uniform, isotropic, elastic medium (Figure 2a). The earthquake sequences on the fault are simulated in their entirety: the nucleation process, the dynamic rupture propagation, post-seismic slip that follows the event, and the interseismic period between events that can last up to tens or hundreds of years (Figure 2b). In all models, the laboratory-derived rate-and-state friction (section 2.1) operates on the fault. Our 1-D fault (Figure 2a) contains a velocity-weakening (VW) region surrounded by velocity-strengthening (VS) regions. The fault slip at the plate rate ($V_{pl} = 10^{-9}$ m/s) is prescribed at the edges of the model. We begin with a standard rate-and-state model but then add thermal pressurization of pore fluids (section 2.2). Parameters for the specific models are listed in Tables 1 and 2.

Table 1
Parameters for All Simulations

Parameter	Symbol	Value
Loading slip rate	V_{pl}	10^{-9} m/s
Shear wave speed	c_s	3,464 m/s
Shear modulus	μ	32 GPa
Reference slip velocity	V_0	10^{-6} m/s
Reference friction coefficient	f_0	0.6

While many events arrest within the VW region, some span the entire VW region (Figure 2b). We refer to the events that span the entire VW region as "complete rupture" events and those that arrest within the VW region as "partial rupture" events.

2.1. Rate-and-State Friction

We use the laboratory-derived rate-and-state laws with the aging law proposed by Dieterich (1979) and Ruina (1983):

$$\tau = (\sigma - p) f = (\sigma - p)\left[f_* + a \ln \frac{V}{V_*} + b \ln \frac{V_* \theta}{L}\right], \tag{1}$$

$$\frac{d\theta}{dt} = 1 - \frac{V\theta}{L}, \tag{2}$$

where σ is the normal stress (constant in time), τ is the shear stress, f is the friction coefficient, V is the slip velocity, p is the pore pressure, θ is the state variable, L is the characteristic slip for the evolution of the state variable, f_* is the reference friction coefficient corresponding to a reference slip rate V_*, and a and b are constitutive parameters. At steady state (constant slip velocity), the values of τ and θ evolve to be their steady-state values τ_{ss} and θ_{ss} given by

$$\theta_{ss}(V) = \frac{L}{V}, \tag{3}$$

$$\tau_{ss} = (\sigma - p)\left[f_* + (a - b) \ln \frac{V}{V_*}\right]. \tag{4}$$

These steady-state relations show that the difference between the parameters a and b controls the fault behavior at steady state. If $(a - b) > 0$, then the fault has velocity-strengthening (VS) friction behavior in which increases in slip velocity result in increases in shear resistance. This leads to stable sliding on the fault

Table 2
Parameters for R + S *Models*

Parameter	Symbol	Standard R + S Model
Fault length along strike	λ	36 km
VW region length (total)	W_{VW}	6 km
VS region length (total)	W_{VS}	24 km
Effective normal stress	$\bar{\sigma} = (\sigma - p)$	50 MPa
Rate-and-state direct effect (VS)	a	0.019
Rate-and-state evolution effect (VS)	b	0.015
Rate-and-state direct effect (VW)	a	0.01
Rate-and-state evolution effect (VW)	b	0.015
Characteristic slip	L	0.125–4 mm
Cell size	Δx	0.625–20 m
Cohesive zone	Λ_0	5–150 m
Nucleation size (Rice & Ruina, 1983)	h^*_{RR}	12–400 m
Nucleation size (Rubin & Ampuero, 2005)	h^*_{RA}	30–980 m

Table 3
Parameters for Models with Thermal Pressurization

Parameter	Symbol	12 km VW zone	Model A	Model B
Fault length along strike	λ	72 km	96 km	96 km
VW region length (total)	W_{VW}	12 km	24 km	24 km
VS region length (total)	W_{VS}	60 km	48 km	48 km
Effective normal stress	$\bar{\sigma} = (\sigma - p)$	50 MPa	50 MPa	25 MPa
Thermal diffusivity	α_{th}	10^{-6}m^2/s	10^{-6}m^2/s	10^{-6}m^2/s
Hydraulic diffusivity	α_{hy}	10^{-3}m^2/s	10^{-3}m^2/s	10^{-3}m^2/s
Specific heat	ρc	2.7 MPa/K	2.7 MPa/K	2.7 MPa/K
Half width	w	10 mm	10 mm	10 mm
Coupling coefficient (when TP present)	Λ	0.1 MPa/K	0.1 MPa/K	0.34 MPa/K
Rate-and-state direct effect (VS)	a	0.050	0.050	0.050
Rate-and-state evolution effect (VS)	b	0.003	0.003	0.003
Rate-and-state direct effect (VW)	a	0.010	0.010	0.010
Rate-and-state evolution effect (VW)	b	0.015	0.015	0.015
Characteristic slip	L	2 mm	2 mm	1 mm
Cell size	Δx	5 m	3.3 m	3.3m
Cohesive zone	Λ_0	75 m	75 m	75 m
Nucleation size (Rice & Ruina, 1983)	h^*_{RR}	200 m	200 m	200 m
Nucleation size (Rubin & Ampuero, 2005)	h^*_{RA}	490 m	490 m	490 m

under steady loading. If $(a - b) < 0$, then the fault has velocity-weakening (VW) behavior. In this case, an increase in slip velocity leads to a decrease in shear resistance, making these regions of the fault potentially seismogenic (Rice & Andy, 1983; Rice et al., 2001; Rubin & Ampuero, 2005).

We first consider models with the standard rate-and-state formulation and no additional dynamic weakening, with parameters given in Tables 1 and 2.

2.2. Enhanced Dynamic Weakening due to Thermal Pressurization of Pore Fluids

Laboratory experiments have shown that the rate-and-state laws (Equations (1)–(4)) work well for relatively slow slip rates (10^{-9} to 10^{-3} m/s). However, at seismic rates of ~1 m/s, additional dynamic weakening mechanisms, such as thermal pressurization, can be present. Thermal pressurization occurs when fluids within the fault heat up, expand, and pressurize during dynamic rupture, reducing the effective normal stress (Noda & Lapusta, 2010; Rice, 2006; Sibson, 1973). The thermal pressurization effect is governed in our model by the following coupled differential equations for pressure and temperature evolution (Noda & Lapusta, 2010):

$$\frac{\partial p}{\partial t} = \alpha_{hy}\frac{\partial^2 p}{\partial y^2} + \Lambda\frac{\partial T}{\partial t}, \tag{5}$$

$$\frac{\partial T}{\partial t} = \alpha_{th}\frac{\partial^2 T}{\partial y^2} + \frac{\tau V}{\rho c}\frac{exp(-y^2/2w^2)}{\sqrt{2\pi}w}, \tag{6}$$

where T is the temperature of the pore fluid, α_{hy} is the hydraulic diffusivity, α_{th} is the thermal diffusivity, τV is the source of shear heating distributed over the shear zone of half-width w, ρc is the specific heat, y is the distance normal to the fault plane, and Λ is the coupling coefficient that gives pore pressure change per unit temperature change under undrained conditions.

The efficiency of the thermal pressurization process depends on the interplay of several of these parameters. Shear heating, τV, must be strong enough to raise the temperature, given both the specific heat of the rock, ρc, and the half-width of the shear zone, w. Furthermore, this heat generation must not be dissipated too quickly by the thermal diffusivity, α_{th}, of the system. If sufficient heat is generated, the temperature of the system increases, and this increase is coupled into an increase in pressure of the fluid. The fluid then pressurizes as long as the hydraulic diffusivity, α_{hy}, is not too large. Several of these parameters are relatively well constrained from laboratory experiments: $\alpha_{th} = 10^{-6}$ m/s, $\Lambda = 0.1$ MPa/K, and $\rho c = 2.7$ MPa/K

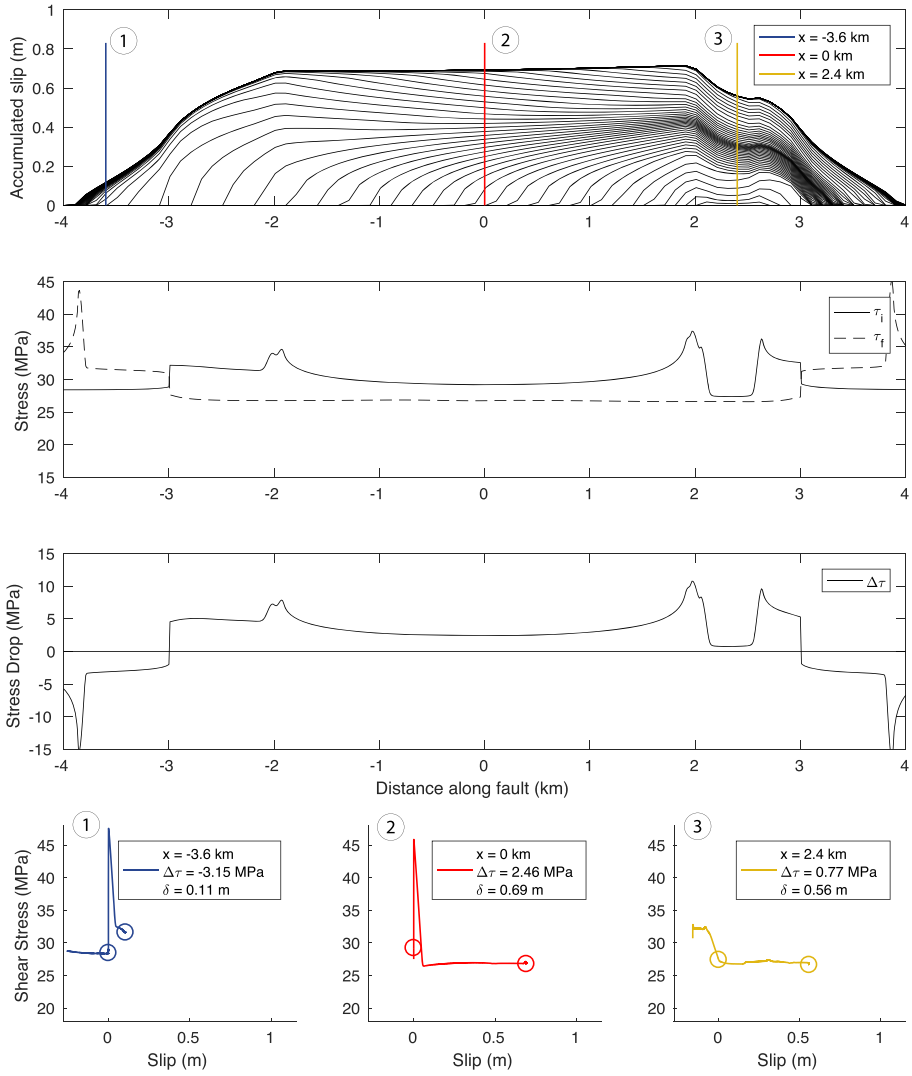

Figure 3. A sample event for the standard rate-and-state fault model. Accumulated slip is plotted every 0.1 s (Row 1). Initial (solid line) and final (dashed line) stress (Row 2) and stress drop distributions (Row 3) are shown along the fault. The stress versus slip evolution at three example points illustrate different behaviors along the fault (Row 4). Initial and final stresses during the event are marked (open circles) for each point, and some previous slip history is also shown preceding the initial stress marker. Point 3 shows the evolution in the nucleation zone, point 1 is in the region where the event arrests, and point 2 shows behavior of a well-established rupture (the majority of the ruptured points experience this behavior). Note that this event is crack-like, and the final stress is nearly equal to the dynamic level of stress for the three representative points.

(Noda & Lapusta, 2010; Rempel & Rice, 2006; Wibberley & Shimamoto, 2005). Thus, the efficiency of the process is effectively controlled by the half-width w and hydraulic diffusivity α_{hy}, which can vary significantly: w can vary from 10^{-3} m to 10^{-1} m and α_{hy} can vary from 10^{-2} m^2/s to 10^{-5} m^2/s (e.g., Rice, 2006). Changing these two parameters within these ranges can make thermal pressurization either very efficient or completely negligible. The values we have chosen are motivated by prior studies (Rice, 2006; Noda & Lapusta, 2010) and are given in Tables 1 and 3.

2.3. Representative Simulated Events

Our simulations produce sequences of dynamic events together with interseismic creep, including aseismic nucleation processes (Figure 2b). However, here, we focus on the properties of individual dynamic events. A sample dynamic event from our simulations is shown in Figure 3. In general, both slip throughout the event and final slip vary along the fault. The spatially varying initial and final shear stress distributions along the fault lead to a stress drop distribution that varies along the fault. Most of the ruptured area

experiences a decrease in shear stress during the event, but both edges of the ruptured area in each of the events show an increase in stress (and hence negative stress drop). The shear stress versus slip evolution along the fault is illustrated for three representative locations. Locations near the nucleation region experience a small coseismic stress drop, with much of the stress change at these points achieved aseismically, during nucleation. Points near the middle of the ruptured area show the expected increase in stress to a peak value, followed by a drop, controlled by our rate-and-state laws, down to some near constant (Figure 3) dynamic value. Where the event arrests, points only slip a small amount and do not completely weaken down to the expected dynamic level of shear stress.

Observations of natural earthquakes cannot resolve these fine variations in stress, slip, slip rate, etc. at all points along the fault as we are able to do in our simulations. Thus, natural events are often described by a single, average value for stress drop and average final slip. In the next sections, we discuss the condensing of heterogeneous slip and stress-drop distributions into average values for the seismic events.

3. Computation of Stress Drops and Breakdown Energy

We follow the averaging methodologies described in Noda et al. (2013), modified to fit our two-dimensional model, since our relevant variables are scalar fields rather than vector fields. The initial distribution of shear traction on the fault before an earthquake is denoted by $\tau_i(x)$. An earthquake produces a slip distribution $\delta(x)$ and the traction along the fault changes to $\tau_f(x)$. The stress drop distribution is defined as

$$\Delta\tau(x) = \tau_i(x) - \tau_f(x). \tag{7}$$

3.1. Averaging of Stress Drop Distribution Based on Seismic Moment

Seismologically estimated values of average stress drop are often based on the seismic moment M_0 of the event as well as the fault dimensions; the following formula is typically used (Kanamori & Anderson, 1975):

$$\overline{\Delta\tau}_M = C\frac{M_0}{\rho^3} = C\frac{M_0}{A^{3/2}}, \tag{8}$$

where A is the ruptured area, $\rho = A^{1/2}$ is the characteristic spatial dimension, and C depends on the shape and aspect ratio of the ruptured domain: $C = 2.44$ for a circular ruptured area and increases for rectangular areas with larger aspect ratios (Noda et al., 2013).

If the actual stress drop is uniform over the ruptured domain Σ, then $\overline{\Delta\tau}_M$ is exactly equal to that value. However, as evident for our example events (section 2.3), the stress drop across the fault is heterogeneous and given by the distribution $\Delta\tau(x)$. In this case, $\overline{\Delta\tau}_M$ is a weighted average of $\Delta\tau(x)$. This average is weighted by the (elliptic) slip distribution E^{12} that gives a uniform stress drop over the same ruptured domain (Madariaga, 1979):

$$\overline{\Delta\tau}_M = \frac{\int_\Sigma \Delta\tau E^{12} d\Sigma}{\int_\Sigma E^{12} d\Sigma}. \tag{9}$$

3.2. Spatial Averaging of Stress Drop

The spatially averaged stress drop can be expressed as the integral of the stress drop of all ruptured points along the fault divided by the ruptured domain Σ:

$$\overline{\Delta\tau}_A = \frac{\int_\Sigma \Delta\tau d\Sigma}{\int_\Sigma d\Sigma}. \tag{10}$$

The stress change at every point has equal weighting of one in this averaging method, unlike $\overline{\Delta\tau_M}$ where E^{12} weights points differently along the fault. Similarly to $\overline{\Delta\tau}_M$, $\overline{\Delta\tau}_A$ depends only on points in the ruptured domain. Considering the entire fault can result in severely underestimating the average stress drop of the event.

The ruptured domain Σ is defined as the region with non-zero slip (which is a line for our model, but a 2-D area in general):

$$\Sigma = \{x \in L | \delta(x) > 0\}. \tag{11}$$

However, it is difficult to precisely determine Σ for observed events due to non-uniqueness and smoothing when finding a solution to an inverse problem. Furthermore, in our models, the fault is prescribed to creep outside the locked, velocity-weakening region, and thus, there is small non-zero slip everywhere on the fault during every event. It is appropriate to only consider points where the inertial term becomes significant, but there is no exact quantitative criterion to define that, so we instead approximate this by defining the ruptured domain Σ to consist of locations that exceed a slip rate of 0.1 m/s during the event:

$$\Sigma = \{x \in L | V(x) > 0.1 \text{ m/s}\}. \tag{12}$$

Altering the seismic velocity threshold may change the effective rupture size. However, there is a sharp falloff in slip rate outside the ruptured area down to the creeping rate many orders of magnitude below the seismic slip rate. Thus, changing this threshold by even an order of magnitude does not change the rupture size appreciably.

3.3. Averaging of Stress Drop Distribution Based on Energy Considerations

The third method of averaging $\Delta\tau(x)$ is consistent with energy partitioning (Noda & Lapusta, 2012; Noda et al., 2013). This stress drop is also part of the averaged shear stress versus slip evolution curve that conserves both the total strain energy released ΔW as well as the dissipated energy E_D as discussed in section 3.4. Here, the final slip distribution $\delta_f(x)$ is used as the weighting function:

$$\overline{\Delta\tau}_E = \frac{\int_\Sigma \Delta\tau\delta_f(x)d\Sigma}{\int_\Sigma \delta_f(x)d\Sigma}. \tag{13}$$

In this method, the ruptured domain is implicitly defined by the slip distribution $\delta_f(x)$.

The three averaging methods ((9)–(10)) and (13) give similar but not identical results for the average stress drop for a given event. Noda et al. (2013) proved that $\overline{\Delta\tau}_E \geq \overline{\Delta\tau}_M$ and observed that $\overline{\Delta\tau}_M \geq \overline{\Delta\tau}_A$ in their simulations. Given that computing seismic moment on our 1-D faults requires additional assumptions of rupture aspect ratio and shape, we focus on computing the energy-based stress drop $\overline{\Delta\tau}_E$ and the spatially averaged stress drop $\overline{\Delta\tau}_A$ in this study, where the moment-based stress drop would be expected to lie in between these two values. For similar reasons, in this study, we present relationships between average stress drop and average slip, rather than moment. Examining these scaling relationships in 3-D calculations is a topic for future work.

3.4. Calculation of Energy Balance and Breakdown Energy *G* in Simulations

In our dynamic simulations, the slip and stress evolution is determined at every point along our fault at all times. As such, we are able to calculate the breakdown energy directly in our model. This can be done by integrating the breakdown energy along the fault for all ruptured points. Furthermore, we can construct a representative average curve for the event and use it to illustrate the breakdown energy.

In the earthquake energy budget per unit area, illustrated in Figure 4, the total strain energy released, $\Delta W/A$, is partitioned into dissipated energy per unit area, E_D/A, which is the area underneath the stress-slip curve, and radiated energy E_R/A:

$$\Delta W/A = E_D/A + E_R/A. \tag{14}$$

We write the balance per unit area because the breakdown work, G, is defined per unit area. The total strain energy released $\Delta W/A$ is given by

$$\Delta W/A = \frac{1}{2}(\bar{\tau}_i + \bar{\tau}_f)\bar{\delta}_f \tag{15}$$

$$\bar{\tau}_i = \frac{\int_\Sigma \tau^i(x)\delta_f(x)dx}{\int_\Sigma \delta_f(x)dx}, \tag{16}$$

$$\bar{\tau}_f = \frac{\int_\Sigma \tau^f(x)\delta_f(x)dx}{\int_\Sigma \delta_f(x)dx}, \tag{17}$$

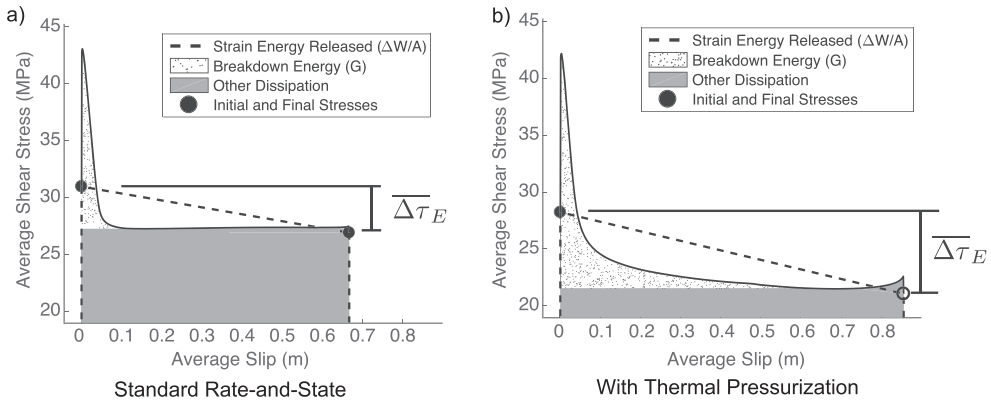

Figure 4. Illustration of the earthquake energy budget and average stress drop using average energy-based shear stress versus slip curves. (a) The average curve for the single event in a standard rate-and-state model from Figure 3. The shear resistance weakens to a nearly constant dynamic value. (b) The average curve for the single event with enhanced dynamic weakening from Figure 9. The fault continues to weaken by more than an additional 5 MPa as it accumulates slip, leading to a larger breakdown energy. In both (a) and (b), the energy-based static stress drop $\Delta\tau_E$ is the difference between the average initial and final shear stresses. The total strain energy released $\Delta W/A$ is outlined by the black dashed line; the associated trapezoid ends at the x axis (not shown). The dissipated energy E_D/A is given by the total area underneath the stress versus slip curve (dotted + gray). Breakdown energy G is the subset of the dissipated energy labeled by the dotted area. Radiated energy can be calculated by subtracting total dissipated energy from the total strain energy released.

where $\bar{\delta}_f$ is the average final slip for the event, $\bar{\tau}_i$ is the average initial shear stress weighted by the final slip, and $\bar{\tau}_f$ is the average final shear stress. For our 1-D fault, let us define the edges of the ruptured domain Σ as L_1 and L_2. Then the dissipated energy can be computed as

$$E_D/A = \frac{1}{L_2 - L_1}\int_{L1}^{L2}\left[\int_0^{\delta_f}\tau(\delta)d\delta\right]dx. \tag{18}$$

The remainder of the total strain energy released is the radiated energy:

$$E_R/A = \Delta W/A - E_D/A. \tag{19}$$

The dissipated energy E_D/A can further be partitioned into the breakdown energy G (Palmer et al., 1973; Rice, 1980) and frictionally dissipated energy E_F/A which makes up the remainder (labeled as "other dissipation" in Figure 4):

$$E_D/A = G + E_F/A. \tag{20}$$

The breakdown energy G_a is analogous to the fracture energy of fracture mechanics and can be calculated as

$$G_a = \frac{1}{L_2 - L_1}\int_{L1}^{L2}\left[\int_0^{\delta(\tau_{min}(x))}(\tau(\delta) - \tau_{min}(\delta))d\delta\right]dx, \tag{21}$$

where we use G_a to indicate the "actual" or on-fault value of G.

One can illustrate the energy balance by a representative average shear stress versus slip curve (Figure 4). We follow the averaging methodology of Noda and Lapusta (2012) to perform this calculation, which involves taking the stress versus slip evolution of every ruptured point and averaging them in slip rather than in time. Thus, this can only be done once the event is complete, and the stress versus slip evolution is known everywhere. The averaging method preserves total strain energy released $\Delta W/A$ and total dissipated energy E_D/A. Every ruptured fault location has, in general, a different amount of total slip $\delta_f(x)$, so the stress versus slip curves at each point are scaled in slip by $\bar{\delta}_f/\delta_f(x)$ so that each point has the same average slip $\bar{\delta}_f$. Then the stress values are scaled by the factor of $\delta_f(x)/\bar{\delta}_f$, thus preserving the areas representing E_D. Once all shear stress versus slip curves are scaled, the stress values at each value of slip are averaged among the curves. We can then calculate our energy quantities from this average curve. The strain energy released per unit area

$\Delta W/A$ is given by the trapezoid indicated by the dashed line in Figure 4, and the dissipated energy per unit area E_D/A is given by

$$E_D/A = \int_0^{\bar{\delta}_f} \bar{\tau}(\bar{\delta}) d\bar{\delta}. \tag{22}$$

One can also compute the quantity motivated by the breakdown energy from the average curve, here titled as G_{curve}:

$$G_{curve} = \int_0^{\bar{\delta}(\bar{\tau}_{min})} (\bar{\tau}(\bar{\delta}) - \bar{\tau}_{min}) d\bar{\delta}. \tag{23}$$

The average curve construction has been shown to preserve total strain energy released $\Delta W/A$ and dissipated energy E_D/A (Noda & Lapusta, 2012). However, it does not necessarily preserve the breakdown energy as the minimum shear stress of the average curve does not have a simple relation to the minima of the curves of each ruptured point. We later show that G_a has a similar, but not identical, value to G_{curve} for the crack-like ruptures considered in this study, and hence, G_{curve} can be used to visualized G_a.

Note that G_a and G_{curve} have units of energy per unit area, while $\Delta W, E_D$, and E_R denote the energies per event and have units of energy. Representations of the type shown in Figure 4 show energies per unit area, and that is why we have been considering quantities $\Delta W/A, E_D/A$, and E_R/A. To compute the corresponding energies per event, one needs to multiply them by the total ruptured area.

3.5. Stress Drop $\overline{\Delta\tau}$ and Breakdown Energy G from Observations

We seek to match the observed trends of magnitude-invariant stress drop and increasing breakdown energy G with increasing event size (Abercrombie & Rice, 2005; Ide & Beroza, 2001; Viesca & Garagash, 2015). However, as discussed earlier, these values cannot be directly measured in observed events and instead must be inferred from other observations.

Stress drop is often calculated using the moment-based average (Equation (9)). For large events, the rupture shape and dimension is found from finite-fault inversions (Kanamori & Brodsky, 2004, and references therein). For small events, for which finite-fault inversions are not feasible, the spectral representation of the seismic waveforms is fitted by a model based on a circular crack with constant rupture speed to obtain the long-period displacement amplitude Ω_0 and corner frequency f_c measurements. These parameters are then used to calculate M_0 from Ω_0 (Brune, 1970) and the source radius r from f_c assuming a circular rupture and constant rupture velocity of $0.9c_s$ (Madariaga, 1976).

The breakdown energy can be estimated from observations as follows (Abercrombie & Rice, 2005):

$$G' = \frac{\bar{\delta}}{2}\left(\overline{\Delta\tau} - \frac{2\mu E_R}{M_0}\right), \tag{24}$$

where G' is the approximation for the breakdown energy G, $\overline{\Delta\tau}$ is the seismologically estimated (static) stress drop, μ is the shear modulus of the rock material, $\bar{\delta}$ is the average slip of the event, M_0 is the seismic moment, and E_R is the radiated energy. The relationship between of G' and the average breakdown energy assumes that (1) the initial stress is the peak stress and (2) that there is no stress overshoot or undershoot at the end of the event, making it potentially different from the actual G (see Figure 2 of Abercrombie & Rice, 2005). We refer to this G' as seismologically estimated breakdown energy G_{SE}.

4. Stress Drops and Breakdown Energy in Earthquake Sequence Simulations on Faults with Standard Rate-and-State Friction Only

4.1. Theoretical Predictions for Breakdown Energy and Stress Drops on Rate-and-State Faults

Based on previous studies and theoretical considerations (Ampuero & Rubin, 2008; Cocco & Bizzarri, 2002; Lapusta & Liu, 2009; Rubin & Ampuero, 2005), we expect both the breakdown energy and the static stress drop to remain approximately the same for events of different sizes on a fault with uniform rate-and-state properties. This is because, at the rupture tip, the fault governed by the standard rate-and-state formulation behaves essentially as one governed by linear slip-weakening friction:

$$\begin{aligned} &\tau_{LSW} = \tau_p - W(\delta - \delta_{ini}) \text{for} \delta - \delta_{ini} \le D_c, \\ &\tau_{LSW} = \tau_d \text{for} \delta - \delta_{ini} > D_c. \end{aligned} \tag{25}$$

where τ_{LSW} refers the linear slip weakening evolution of shear stress from the peak shear stress, τ_p, at initial slip δ_{ini} to the dynamic level of shear resistance τ_d over the critical slip-weakening distance D_c. The weakening rate W is defined as

$$W = \frac{\tau_p - \tau_d}{D_c}. \tag{26}$$

For the standard rate-and-state formulation, one can write the initial stress τ_i from (1):

$$\tau_i = \bar{\sigma}\left[f_* + a\ln\frac{V_{ini}}{V_*} + b\ln\frac{V_*\theta_{ini}}{L}\right]. \tag{27}$$

As slip rate abruptly increases from near-zero V_{ini} to dynamic V_{dyn} at the crack tip, stress will increase to some peak value τ_p, which can be approximated by

$$\tau_p = \tau_i + a\bar{\sigma}\ln\frac{V_{dyn}}{V_{ini}}. \tag{28}$$

Assuming that the slip acceleration occurs at negligible slip and hence with no state evolution. As slip accumulates, the stress further evolves to a steady-state dynamic level given by

$$\tau_d = \tau_{ss}(V_{dyn}) = \bar{\sigma}\left[f_* + (a-b)\frac{V_{dyn}}{V_*}\right]. \tag{29}$$

This weakening effect occurs at weakening rate W:

$$W = \frac{b\bar{\sigma}}{L}, \tag{30}$$

and hence, the evolution occurs over the effective critical slip-weakening distance D_c given by

$$D_c = \frac{\tau_p - \tau_d}{W} = L\ln\frac{\theta_{ini}V_{dyn}}{L}. \tag{31}$$

If the final stress is approximately equal to the dynamic resistance, then we expect:

$$\Delta\tau = \tau_i - \tau_d = \bar{\sigma}\left[a\ln\frac{V_{ini}}{V_*} + b\ln\frac{V_*\theta_{ini}}{L} - (a-b)\ln\frac{V_{dyn}}{V_*}\right] \tag{32}$$

$$G = \frac{1}{2}\left(\tau_p - \tau_d\right)D_c = \frac{1}{2}b\bar{\sigma}L\left(\ln\frac{\theta_{ini}V_{dyn}}{L}\right)^2. \tag{33}$$

These quantities depend on the dynamics of the process through V_{ini}, V_{dyn}, and θ_{ini}, but this is a weak dependence since they are contained within logarithms and changes of even an order of magnitude alter the final product by only a small amount. There is a much stronger dependence on the friction parameters a, b, and L, which are constant in a given model.

4.2. Dependence of G and $\Delta\tau$ on Magnitude for Given a, b, and L

Indeed, our simulations show that for uniform frictional parameters a, b, and L along the fault, both G_a and $\Delta\tau$ are nearly constant for events of different sizes. Both trends are evident in the accumulated slip profiles and average curves for three events of different sizes from the same simulation of earthquake sequences (Figure 5). Larger events accumulate more slip and rupture longer fault stretches, but the breakdown energy (dotted area) and static stress drop are nearly equal for the three illustrated events.

There are some slight trends in G and $\overline{\Delta\tau}$ due to the dynamics of the process. Larger events tend to have lower average initial stresses, due to rupturing longer fault stretches, building more stress concentration, and entering slightly less favorably stressed regions. All events weaken down to approximately the same dynamic level, as expected. This leads to a mild decrease in the static stress drop from $\overline{\Delta\tau_E} = 3.3$ MPa for the smallest event down to $\overline{\Delta\tau_E} = 1.8$ MPa for the largest event. The peak stress τ_p slightly increases with the event size, due to more stress concentration during the larger event and higher initial values for the state variable θ_{ini} from longer recurrence times. The outcome is slightly higher breakdown energies as the

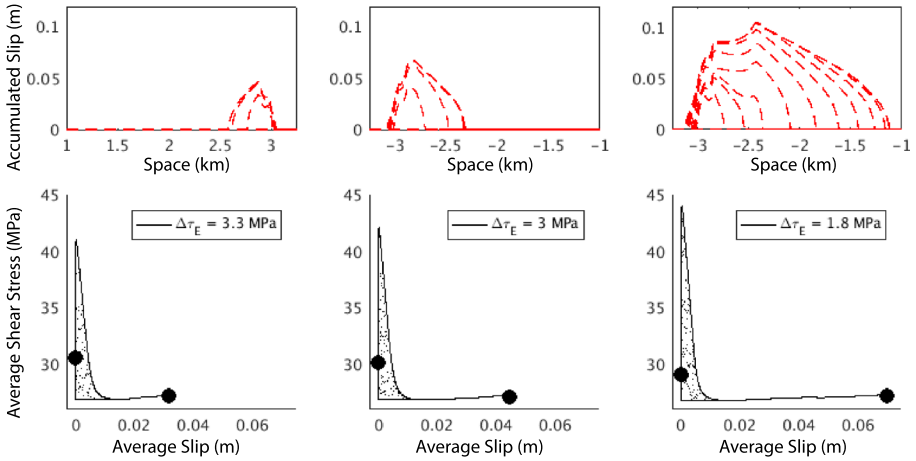

Figure 5. Three sample events of different sizes from the standard rate-and-state simulation with $L = 250$ μm. (Top) Accumulated slip profiles illustrate the total slip along the fault as well as the spatial extent of the rupture. (Bottom) Average shear stress versus slip curves illustrate the average behavior on the fault during the event. The initial and final stresses are marked by circles; the breakdown energy is indicated by the dotted area. For a given value of L, the breakdown energy remains nearly constant. The stress drop slightly decreases, and the breakdown energy slightly increases with the event slip, as discussed in the text. These three events are marked with gray, downward-pointing triangles in Figure 6.

event size increases. However, these two effects produce relatively small variations, within a factor of two, in both G and $\Delta\tau$.

We find that these trends extend for all events in our simulations (Figures 6 and 7a). For $L = 250$ μm (black circles), events differ by nearly an order of magnitude in slip, from 0.01 m to 0.1 m. The corresponding stress drops are nearly constant, around 2–3 MPa, with a slight decreasing trend with the increasing event size. The breakdown energies are also approximately constant, with a slight increasing but saturating trend (Figure 7a) for all events.

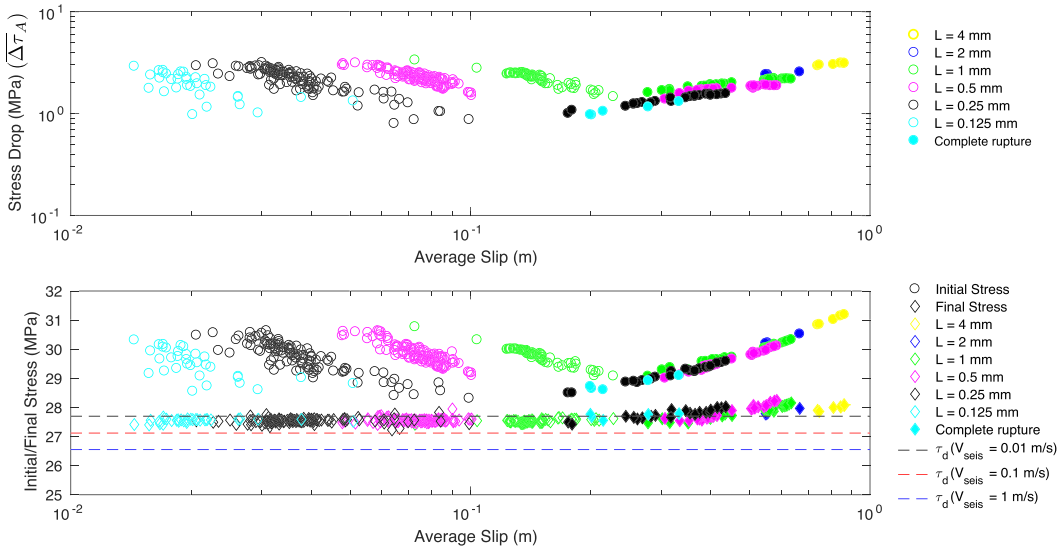

Figure 6. (Top) Stress drops $\overline{\Delta\tau_A}$ for events from several simulations with standard rate-and-state friction and L ranging from 0.125 mm to 4 mm (no dynamic weakening). Complete rupture events are marked with filled-in shapes. The stress drops do not vary with L. (Bottom) Average initial and final stresses for each event from the same simulations. Average final stresses are similar for all events and agree with the expected dynamic levels of stress for V_{dyn} = 0.01–0.1 m/s.

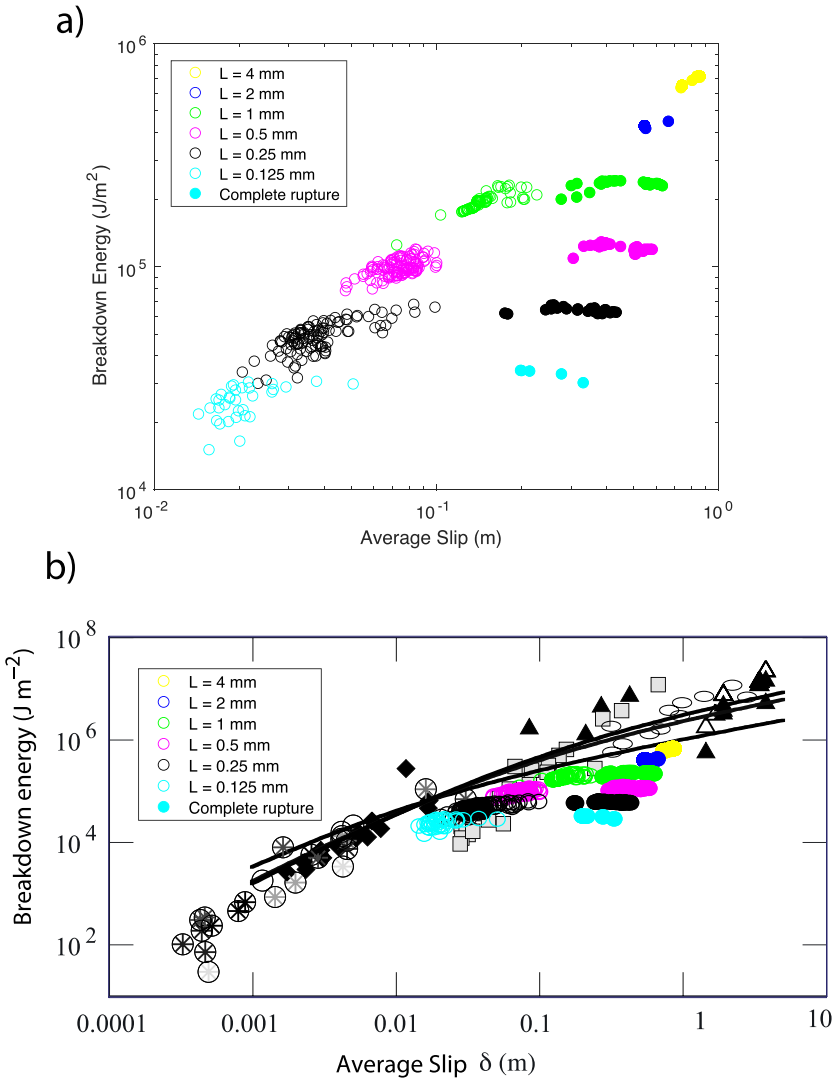

Figure 7. (a) Breakdown energies G_a for events from several simulations with standard rate-and-state friction and L ranging from 0.125 mm to 4 mm (no enhanced dynamic weakening). Complete rupture events are marked with filled-in shapes. Increasing L leads to an increase in the breakdown energy. But breakdown energy only slightly increases and saturates for events with the same L. The two largest values of L lead to almost exclusively complete rupture events because the nucleation size is too large to produce small events given the size of the VW region. (b) Breakdown energies from simulated events overlaid on observational inferences for natural events from Rice (2006). The values are similar, though systematically lower, and the standard rate-and-state model produces breakdown energies that do not increase at the same rate as those inferred from natural events.

The example event discussed earlier (Figure 3) shows the expected behavior for the standard rate-and-state case. This event has the area-averaged stress drop of $\overline{\Delta\tau}_A = 2.4$ MPa, which matches well with the stress drop distribution seen in Figure 3. The entire ruptured domain is plotted in Figure 3, including penetration into the velocity-strengthening region. This is evident from the negative stress drops found at the edges of the event, greater than 3 km away from the center of the fault. Three representative points are chosen to show the variability of the stress versus slip evolution along the fault. The point at 2.4 km is in the nucleation zone and experiences mostly aseismic stress evolution (solid line preceding initial stress point) followed by little coseismic stress change with slip. The point in the arrest zone (−3.6 km) shows a very different behavior, with an increase to a peak level and a drop. However, the stress drop is negative (stress increase), owing to the velocity-strengthening properties of the fault at this point. The point at the center of the fault (0 km) is representative of the behavior of the majority of the fault. This point shows the typical rate-and-state behavior with an increase to a peak level of stress followed by a drop to a near-constant dynamic level of stress. This point experiences a stress drop similar to the average for the entire event. All of the points

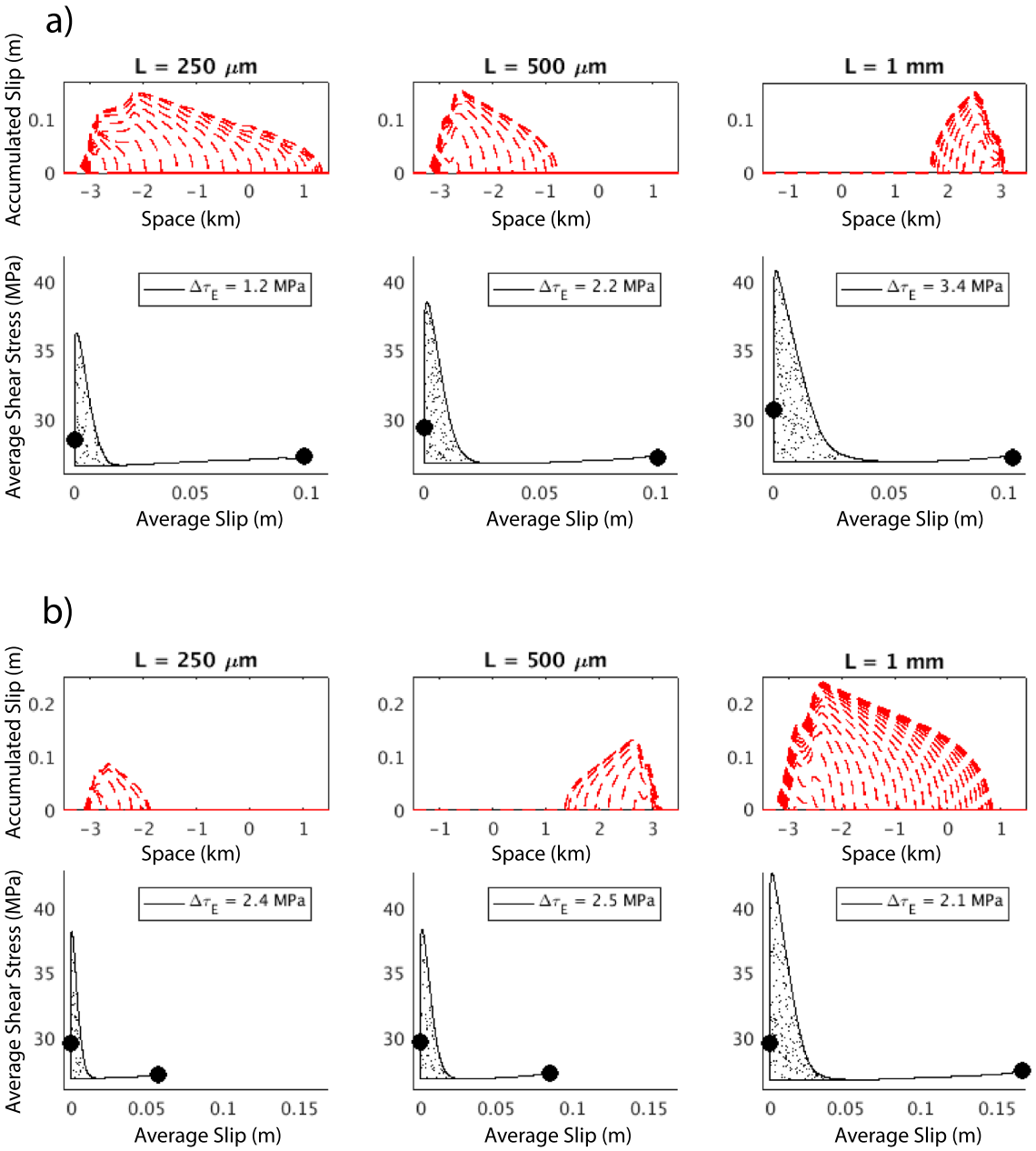

Figure 8. (a) Three sample events with comparable average final slip from rate-and-state simulations with different L. (Row 1) Accumulated slip profiles illustrate the total slip along the fault as well as the spatial extent of the rupture. (Row 2) Average stress versus slip curves illustrate the average shear stress versus slip behavior on the fault during the event. Increasing L increases both the slip weakening distance D_c as well as the breakdown energy of an event with comparable average final slip. These three events are marked with gray stars in Figure 6. (b) Three sample events with comparable stress drops, but varying final slips, from rate-and-state simulations with different L. (Row 1) Accumulated slip profiles and (Row 2) average stress versus slip curves. Increasing L increases both the slip weakening distance D_c as well as the breakdown energy, but does not affect the average stress drop. These three events are marked with gray upward-pointing triangles in Figure 6.

on the fault are averaged to create the illustrative average curve (Figure 4a). From the average curve, it is apparent that the majority of points follow the behavior qualitatively similar to the point at 0 km. Note that the energy-based stress drop from the average curve is $\overline{\Delta\tau}_E = 4$ MPa, which is higher than the $\overline{\Delta\tau}_A = 2.4$ MPa as expected (Noda & Lapusta, 2012).

4.3. Increasing G and Magnitude-Invariant $\overline{\Delta\tau}$ with Increasing Values of L

Breakdown energy has a weak dependence on the dynamics in a standard rate-and-state fault model, but it has a stronger, quasi-linear, dependence on the characteristic slip distance L. One of the ways to reproduce an

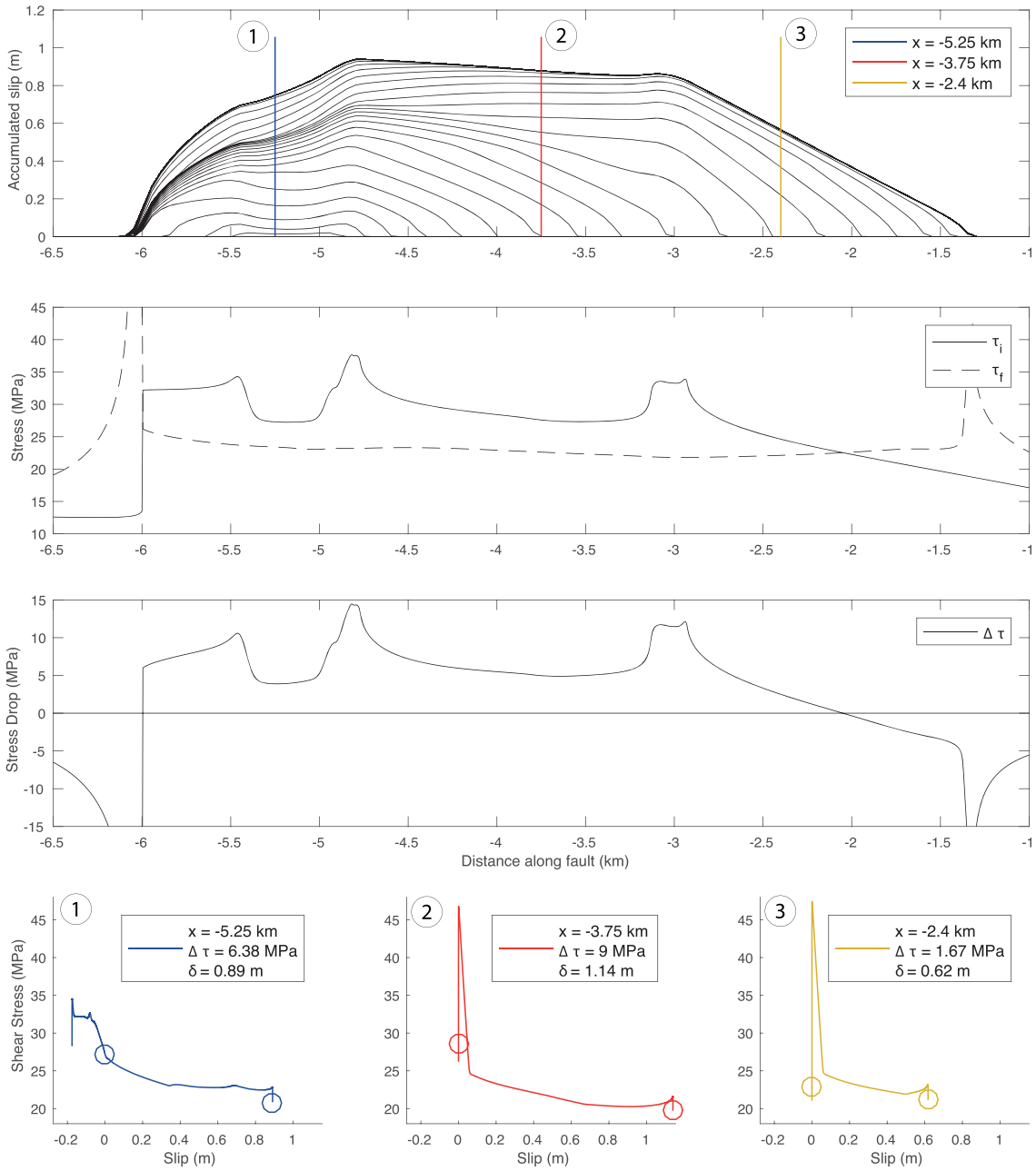

Figure 9. A representative event for the models with thermal pressurization. The plotting conventions are the same as on Figure 3. The three sample points exhibit decreasing dynamic stress with slip throughout the event, illustrating the effect of additional dynamic weakening due to thermal pressurization.

increase in G_a with average slip is to systematically increase L, which also systematically alters the effective critical slip-weakening distance D_c (Figure 8). The peak stress of each event also increases, predominantly due to a longer recurrence time that results in fault strengthening. Increasing L increases the nucleation size of the event, and thus, a stress increase must penetrate further into the VW fault before an event nucleates, leading to a higher initial state variable θ_{ini}, higher initial stress τ_i, and higher peak stress τ_p. This is even the case for events with the same amount of average slip (Figure 8a). However, the increase in the critical slip-weakening distance is clearly the main contributing factor to the increased G_a. The dynamic levels of stress are nearly constant in all three cases as expected; this level does not directly depend on L. The stress drops increase with increasing L for these three events, due to the fact that we have chosen three events with very similar slips (Figure 6a, star symbols). Stress drops for the entire sequence of events do not change as

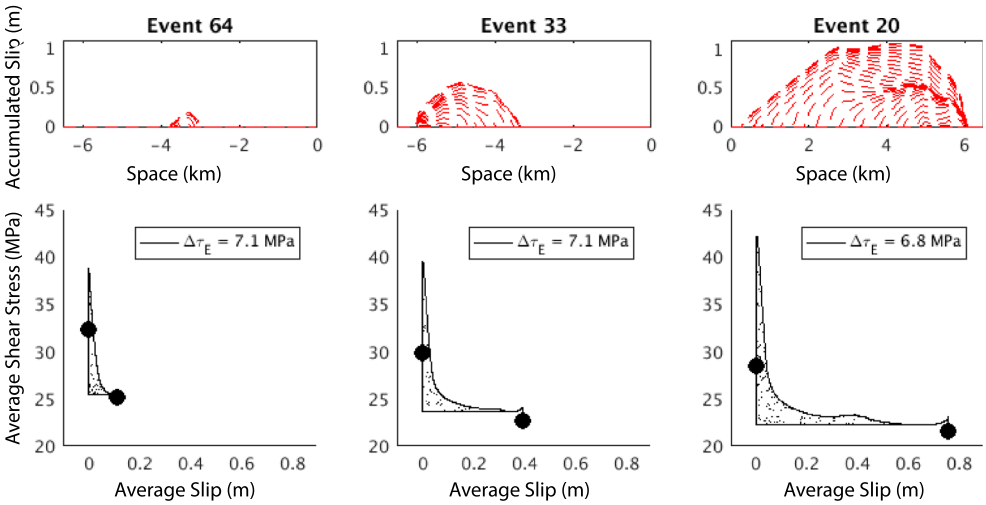

Figure 10. Three sample partial rupture events from the same simulation with a 12-km-long velocity-weakening region and thermal pressurization. (Top) Accumulated slip profiles of the three events. (Bottom) Average shear stress versus slip curves. The initial and final stresses are marked by circles; the breakdown energy is indicated by the dotted area. As event size increases, both the average initial stress and average final stress decrease, so that the stress drops remains nearly constant at ~7 MPa.

we increase L (Figure 6a). This is illustrated by selecting three other events that no longer have the same average final slip (Figure 8b), but do have comparable stress drops.

Varying L over an order of magnitude from 125 μm to 4 mm leads to a clear increase in breakdown energy (Figure 7a) that is much larger than the slight increasing trend we find for larger events of a given L. There are clear groups of events with similar breakdown energies, corresponding to simulations with each value of L. The values for the breakdown energies compare favorably to those from Rice (2006), though they are systematically lower, particularly at higher values of slip (Figure 7b). For a given L, the simulated breakdown energies level off and do not capture the observed trend. Even increasing L is not completely sufficient to match the observed trend.

Simulations with all values of L have comparable stress drops, determined by values of σa and σb. All of our calculated stress drops fall into the 1–3 MPa range which is consistent with inferred stress drops from natural events. We find two distinct trends when separating partial rupture from complete rupture events (Figure 6). The first trend is that the partial rupture events show a slight decrease in stress drop with increasing slip. This is because all events arrest at similar levels of average final stress. However, as discussed in the previous section, larger events initiate with slightly lower average levels of prestress (unless they are complete ruptures, as discussed below) and thus have smaller stress drops. The second is for the complete rupture events; these events have the same ruptured domain, and the ones with larger slip correspond to larger stress drop, reflecting variability in the prestress level for complete rupture events. Note that, for each particular value of L, the decrease in stress drop with slip is within a factor of 3; however, the distribution of stress drops across the full set of events for all values of L is nearly magnitude-invariant, with a scatter well within that inferred for natural earthquakes.

5. Nearly Magnitude-Invariant Stress Drops and Increases in Breakdown Energy in Earthquake Sequence Simulations with Thermal Pressurization

We consider a 12-km-long VW segment surrounded by two 24-km-long VS sections and then increase our seismogenic zone from 12 km to 24 km in order to further expand the range of the simulated event sizes. Extending our fault to 24 km allows for a greater range of event sizes, with slips ranging from ~0.07 m to ~10 m.

Our simulations with a 12-km-long VW segment produce a range of events, with average slips of 0.1 m up to 5 m. One of the events is illustrated in more detail in Figure 9. It nucleates in an area of higher prestress and propagates along the fault until it reaches lower levels of prestress that are unfavorable enough to arrest the

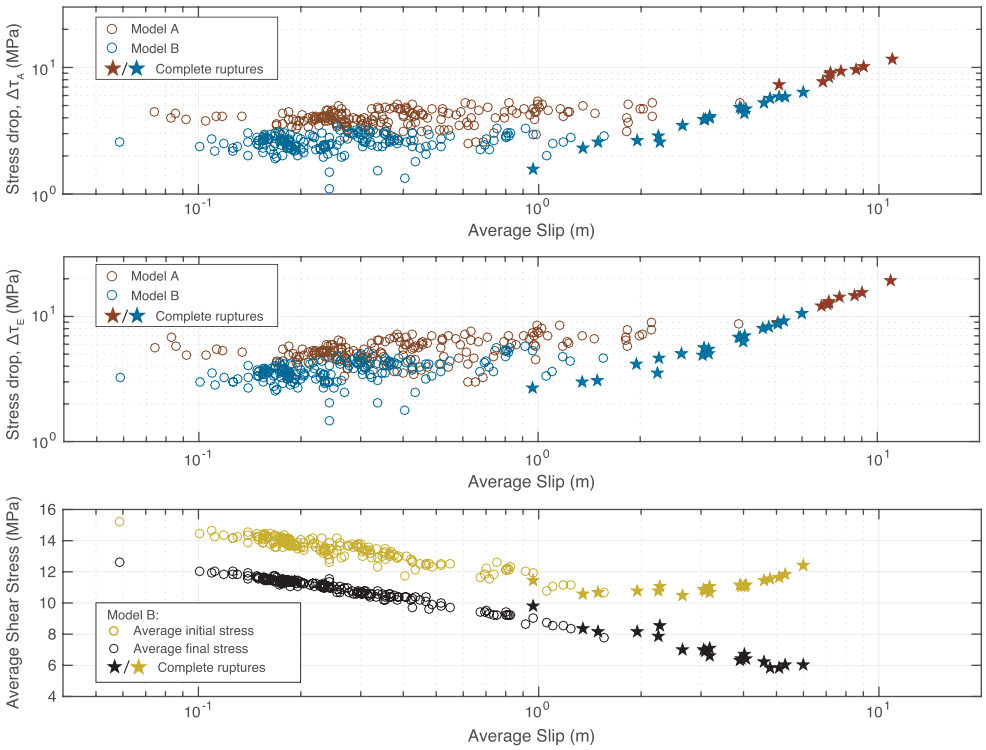

Figure 11. Stress drops $\overline{\Delta\tau_A}$ (top) and $\overline{\Delta\tau_E}$ (center) for events in the simulation with thermal pressurization and a 24-km-long velocity-weakening region. Events with complete ruptures are denoted by stars. (Bottom) Spatially averaged initial stress $\bar{\tau}_i$ and final stress $\bar{\tau}_f$ in the simulation with thermal pressurization and a 24-km-long fault. Partial rupture events exhibit a decrease in both average initial and final stresses with increasing slip such that the change in average stress drop is relatively minor over a decade increase in average slip, resulting in nearly magnitude-invariant stress drops. Parameters from linear fits between the average stress drops and the logarithm of average slip are given in Table 4.

event. The shear stress versus slip behavior is shown for three representative points. All three points show continuous weakening with slip, illustrating that thermal pressurization is acting effectively along the entire fault. The point in the nucleation zone (−5.25 km) again shows significant aseismic stress evolution (solid line preceding the initial stress point), followed by lesser coseismic stress change with slip. The other two points along the fault (−3.75 km and −2.4 km) show the expected behavior for most ruptured points with an initial increase and rapid decrease in stress (similar to the standard rate-and-state behavior) followed by a continuous decrease in stress with slip (due to dynamic weakening from thermal pressurization). The average curve for this event (Figure 4b) shows the behavior similar to the points outside the nucleation zone. Note that this event, as are others in our models, is largely crack-like, that is, have local durations of slip which are comparable to the overall rupture duration.

To illustrate how stress drop and breakdown energy vary with the event size, we consider three representative events with progressively larger average slip (Figure 10). The smallest event (Event 64) has the highest average prestress and also the highest average final stress. The intermediate-size event (Event 33) has a lower prestress, and it weakens more so it also has a lower final stress. The largest event (Event 20) has the lowest average initial stress, and it weakens the most, so it also has the lowest average final stress. As a result, all three events have approximately the same stress drop $\overline{\Delta\tau_E}$ of 7 MPa. As the average slip of the events increases, so does the breakdown energy (Figure 10). This increase in the breakdown energy is due to the additional dynamic weakening, as expected, based on considerations in Rice (2006).

Let us consider the stress drops for all events, using the 24-km fault models. Both energy-based stress drops $\overline{\Delta\tau_E}$ and area-averaged stress drops $\overline{\Delta\tau_A}$ are calculated (Figure 11). For the partial rupture events, the stress drops appear approximately constant, for the average slips ranging from 0.05 m to 2 m. The energy-based stress drops are higher than the area-averaged ones, consistent with Noda et al. (2013). We perform a linear fit between both the spatial and energy-based average stress drops and the logarithm of the average slip

Table 4
Parameters From Linear Fit to Trends in Average Stress Drop and Log-10 Slip, as Shown in Figure 11

Model set	Slope (MPa/$\log_{10}$(m))	Intercept (MPa)	STD (MPa)
Spatially-averaged stress drop			
Model A, partial ruptures	0.6	4.3	0.6
Model B, partial ruptures	0.2	2.7	0.4
Model A, complete ruptures	13.7	-2.9	0.4
Model B, complete ruptures	6.2	1.1	0.4
Energy-based average stress drop			
Model A, partial ruptures	2.0	6.3	1.0
Model B, partial ruptures	1.5	4.6	0.6
Model A, complete ruptures	29.9	-12.6	0.4
Model B, complete ruptures	9.6	1.3	0.8

for sets of partial and complete ruptures (Table 4). The spatially averaged stress drops for partial ruptures in both models exhibit a mild trend with average slip, resulting in a 10% to 20% increase over a decade of average slip. We may illustrate how this would correspond to changes in seismic moment using the common approximation assuming that the stress drops are indeed magnitude-invariant and therefore that the average slip and rupture radius for a circular crack increase linearly with each other, resulting in a cubic relationship between moment and average slip. Thus, a decade of average slip corresponds approximately to three orders of magnitude in seismic moment or two units in moment magnitude. The energy-based average stress drop shows a stronger relationship with average slip, though the increase in stress drop with slip for partial ruptures in both models results in an increase of only around a factor of 1.5 over a decade of average slip. We consider these trends to exhibit near magnitude invariance, since the changes in average stress drop are relatively mild in comparison to the variation in average slip, with the resulting trend most likely not being discernable given the wide scatter and uncertainties in seismological inferences. Moreover, the overall weakening due to thermal pressurization increases far more substantially than the average stress drop with event size (Figure 10).

These findings confirm our hypothesis that larger events weaken more but also tend to occur at lower average initial stress, thus keeping stress drops relatively constant over a range of event sizes. In fact, for the entire sequence of partial rupture events, both average initial and average final stresses decrease with the increasing event size (or slip) (Figure 11). The complete rupture events break the nearly magnitude-invariant trend, exhibiting average stress drops that increase more substantially with event size. However, the stress drops for these events are strongly affect by the properties of the VS region, as further discussed in section 6, and there is a range of VS properties for which these events also exhibit nearly magnitude-invariant stress drops.

Breakdown energy G_a computed using the on-fault quantities from our simulations increases with increasing event size (Figure 12) and matches estimates of breakdown energies for natural events, as expected from the simplified theoretical considerations in Rice (2006). We also compare the true breakdown energy G_a and estimated value G_{SE} for our simulated ruptures. The comparison (Figure 13) shows that the actual and estimated values agree relatively well in the majority of cases, within a factor or two. This is because the ruptures are close to being crack-like, the case for which the estimate of G_{SE} was developed. Moreover, despite the average initial stress not being the same as the peak stress in our simulated ruptures, the estimated value G_{SE} still provides a reasonable representation of the actual average value G_a. The strength excess increases the breakdown energy G_a with expense to the radiated energy E_R/A, so that the seismological estimate (24) still provides an adequate representation for the crack-like ruptures in our simulations. Our preliminary studies with stronger enhanced dynamic weakening that often leads to self-healing pulse-like ruptures (e.g., Noda et al., 2009) shows that G_{SE} is a poor estimate in that case; an alternative estimate for the self-healing pulse-like case has been developed by Viesca and Garagash (2015). Next, comparing G_a to breakdown energy calculated from the average curves G_{curve} we see good, but not perfect agreement (Figure 13). This is expected since the averaging process preserves the total strain energy release and the dissipated energy, but not the minimum dynamic level of stress. Therefore, the averaged curves provides a good illustration of G but not the exact value of it.

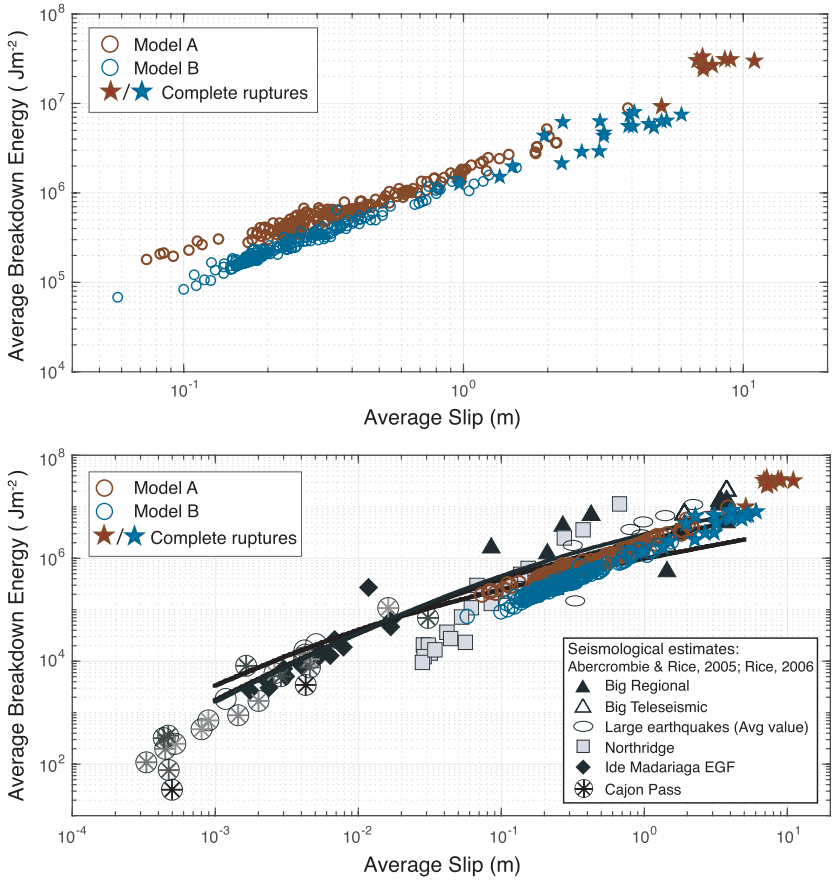

Figure 12. (Top) Breakdown energies G_a for the simulation with thermal pressurization and a 24-km VW region. Complete ruptures are denoted by stars. (Bottom) Breakdown energies from our simulations compared to those inferred for natural events (Abercrombie & Rice, 2005; Rice, 2006). Our models are able to match the trend of the observed events quite well. That data set includes individual estimates for large earthquakes (triangles) from regional and teleseismic recordings, aftershocks from the 1994 Northridge earthquake (squares), averaged values from large earthquakes with several estimates of G′ (ovals), and small earthquakes recorded at depth in the Cajon Pass borehole (circles with asterisks) and Long Valley borehole (diamonds).

The temperatures in our simulated shear zones should remain below melting, for self-consistency of the models, since melting and its consequences are not included in our constitutive relations. Figure 14 illustrates the evolution of the maximum temperature change measured within the 24-km velocity-weakening region. Both Models A and B assume relatively low effective normal stresses of 50 and 25 MPa, corresponding to substantial chronic fluid overpressurization. For Model A, with normal stress of 50 MPa and relatively mild thermal pressurization, the largest events increase the fault temperature by over 2000 K, well above the expected equlibrium melting temperature of 1000 °C for wet granitic compositions in the shallow crust (Rice, 2006). Note that the degree of shear heating during frictional sliding would be even more extreme for models incorporating only rate-and-state friction with comparable effective confining stress, as they would result in higher dynamic levels of shear resistance throughout slip. As we further reduce the effective normal stress and increase the efficiency of thermal pressurization, as in Model B, our models are able to accommodate more reasonable fault temperature fluctuations within 500 K, while maintaining the desired trends in magnitude-invariant stress drops and increasing breakdown energy with event size. Our future work will examine models with more efficient enhanced dynamic weakening with more localized shear, including conditions more consistent with slip on a plane as discussed by Rice (2006).

6. Complete Rupture Events and Effect on Stress Drop of Rupture-Arresting VS Regions

Complete rupture events that rupture all of the VW region tend to have different behavior from partial rupture events. These events do not encounter an area of unfavorable prestress within the VW region, but

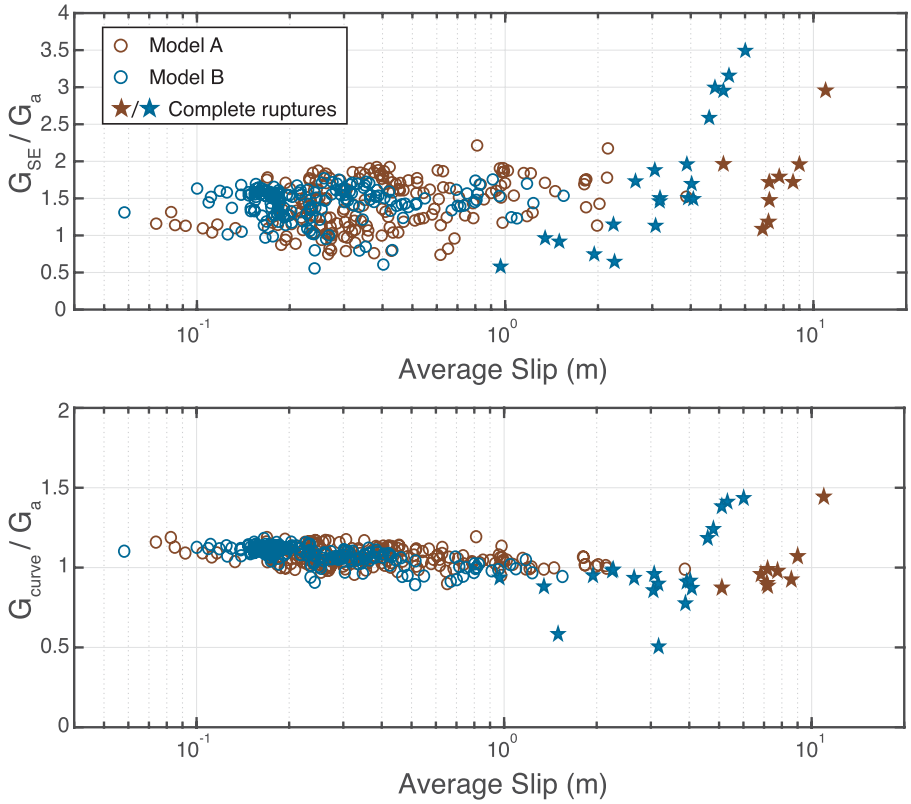

Figure 13. (Top) Comparison of seismically estimated breakdown energy G_{SE} to G_a. There is reasonable agreement for the majority of events. (Bottom) Comparison of breakdown energy calculated from the average curves G_{curve} and actual breakdown energy G_a for the 24-km-long model. The averaged curve provides a good illustration of G but not the exact value of it, as expected.

rather arrest due to the VS barriers. Their spatial extent is approximately equal to the length of the VW region, due to the relatively strong VS barriers adopted, but their slip varies. Hence, their stress drop, which approximately scales with slip divided by the rupture extent, scales with slip, as is evident in Figure 15.

This consideration implies that the stress drop of the complete rupture events can be altered if their extent can vary, due to different lengths of their penetration into the VS barriers. We explore how altering the properties of the velocity-strengthening barrier can affect the stress drops of the complete rupture events using six different models (VS1-VS6) with progressively less velocity-strengthening regions (Table 5). In other words, the VS regions surrounding the VW seismogenic zone become closer to velocity-neutral. We only alter the properties of the VS region; all other parameters match those from Tables 1 and 3. Each model is allowed to produce several complete rupture events and stress drops are plotted against rupture length (Figure 15 top) and average slip (Figure 15 bottom) for each event. We find that the stress drops of these complete rupture events indeed depend on the properties of the VS regions (Figure 15). For models with moderate to relatively strong velocity strengthening regions (VS1-4), the stress drops for partial rupture events are magnitude-invariant over about one order of magnitude increase in slip. However, for models with stronger velocity-strengthening regions (VS1 and VS2), the largest complete rupture events continue to slip more but are unable to propagate appreciably further into the velocity-strengthening regions. As a result, for models with stronger VS regions, larger complete ruptures have increasingly larger stress drops with slip due to the larger degree of slip being confined in nearly the same spatial region.

As we decrease the degree of velocity strengthening in the VS regions, complete rupture events with larger slip propagate further into the VS region and their rupture length increases (Figure 15 top). Correspondingly, the stress drop of these largest complete rupture events decreases. In fact, for models with the least VS regions (VS4-6) the trend for the complete rupture events changes from that of stress drop increasing with their size to a decreasing trend. For less VS regions, the smaller partial rupture events are also able to

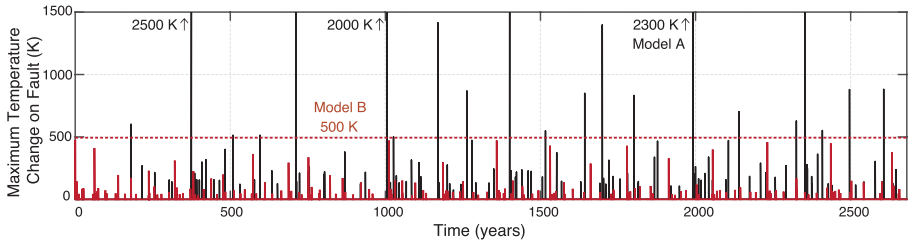

Figure 14. Evolution of the maximum temperature change on the fault measured within the velocity-weakening domain in simulations for Model A (black) and Model B (red). Both models assume relatively low effective normal stresses (50 and 25 MPa, respectively) and hence substantial chronic fluid overpressurization, however to maintain reasonable fault temperatures to avoid melting our models also require efficient thermal pressurization, such as in Model B.

propagate further into the VS region, and thus, their average stress drops decrease as well. For the two models with the least VS regions (VS5 and VS6), we see stress drop slightly decrease with increasing event size for all events. The largest complete ruptures also have the lowest stress drops, close to ~1 MPa. It is clear that the properties of the velocity-strengthening region can have a profound effect on the average stress drops. The exact nature of this effect is best studied in 3-D models with 2-D faults, where the relation of the VS boundary of events to their VW region can be different than in the 1-D faults considered in this work.

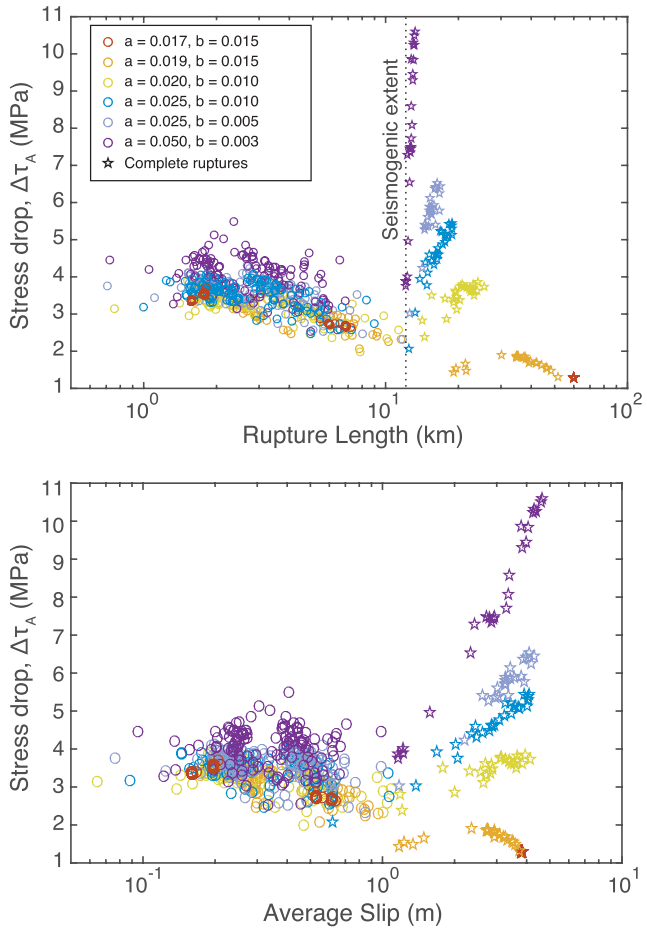

Figure 15. Comparison of stress drops for events produced by six different models with a 12-km-long VW region surrounded by VS regions of different properties. Complete rupture events are indicated by stars. (Top) Stress drops versus rupture length for each event produced in the six simulations. VS regions with lower VS allow for greater rupture penetration and thus longer rupture lengths for the complete rupture events. (bottom) Stress drops versus average slip for the same simulations. Stress drops show nearly magnitude-invariant trend for a range of VS values.

Table 5
Parameters for Models With Different VS Properties

Model	a	b	$(a-b)$
VS1	0.050	0.003	0.047
VS2	0.025	0.005	0.020
VS3	0.025	0.010	0.015
VS4	0.020	0.010	0.010
VS5	0.019	0.015	0.004
VS6	0.017	0.015	0.002

7. Conclusions

We have examined the variations of the average stress drop and breakdown energy with rupture size in fully dynamic simulations of earthquake sequences on rate-and-state faults with and without enhanced dynamic weakening due to the thermal pressurization of pore fluids.

Standard rate-and-state fault models are capable of reproducing realistic stress drops as well as the observationally inferred magnitude invariance in stress drops. However, the breakdown energies depend on the rate-and-state characteristic slip L and increase only slightly with increasing event size for models with a given value of L, before saturating. Simulations with larger L lead to larger values of breakdown energies. However, this alone is not sufficient to match the observed trend, because the nucleation size increases with large L and the models with large L are no longer able to produce small events. This problem can potentially be resolved by using a nonconstant value for L, perhaps one that evolves with slip or slip rate. One can physically motivate this by imagining that the characteristic slip distance evolves as the fault slips and undergoes physical changes including damage on the fault in the form of gouge and off the fault in the form of cracking. These processes may alter the "effective" characteristic slip distance on the fault during the dynamic event. Evolving L during the event may serve as a proxy for these additional phenomena.

Our simulations show that fault models with enhanced dynamic weakening due to thermal pressurization can explain both the increasing trend in breakdown energy with increasing event size as well as the near magnitude invariance of average stress drops. The simulated breakdown energies G_a match well the inferred trend for natural events, and our stress drops are consistent with seismologically inferred values in the 1–10 MPa range for all of our event sizes, excluding the complete rupture events in some models. We find that, with enhanced dynamic weakening, larger partial events result in lower average levels of prestress, due to their penetration into lower-prestressed regions. These events also weaken the fault more than smaller events do and arrest at lower levels of final stress. Our simulations reproduce this effect for events ranging several orders of magnitude in size (two orders of slip and approximately four orders of magnitude in moment).

The thermal pressurization parameters assumed in this work, motivated by values from Noda and Lapusta (2010), result in moderate additional dynamic weakening and crack-like ruptures. Given the assumed frictional properties, in order to maintain reasonable fault temperatures that avoid wholesale melting of the shearing layer for self-consistency of the models, such models do require the assumption of relatively low effective confining stress and hence substantial chronic fluid overpressurization throughout seismogenic depths. Such fluid overpressure may be present on fault, for example, some subduction megathrusts. Models with more substantial dynamic weakening, examined for single rupture events (e.g., Noda et al., 2009), do show that sufficiently enhanced weakening can lead to reasonable fault temperatures even with hydrostatic values of pore pressure; examining such models in terms of earthquake sequences is the subject of ongoing work. Such models would result in relatively sharp self-healing pulses (e.g., Noda et al., 2009), which have been advocated as prevailing rupture modes in some observational studies (Heaton, 1990). Other observational studies inferred broader pulse-like ruptures (e.g., Ye et al., 2016), which could be an observational equivalent of crack-like ruptures with weak tails. Our future work will examine whether models with self-healing pulses also reproduce a range of available observations.

We also find that the properties of the arresting velocity-strengthening regions have an impact on the average stress drop of events that significantly propagate into these regions. This is most important for our complete rupture events. Partial ruptures encounter low levels of prestress which inhibit their propagation and lead

to their arrest within the VW region. Complete ruptures do not encounter unfavorable prestresses which would inhibit their propagation more and instead are held to a limited rupture domain by the VS regions, no matter their slip. Arresting regions with higher values of VS inhibit rupture propagation and lead to increasing stress drops as larger events slip more but are unable to increase in their spatial extent. Lower values of VS allow for significant propagation into the arresting regions and can lead to decreasing stress drops as the rupture area increases.

Acknowledgments
This study was supported by the National Science Foundation (Grants EAR 1142183 and 1520907) and the Southern California Earthquake Center (SCEC), Contribution No. 8128. SCEC is funded by NSF Cooperative Agreement EAR-1033462 and USGS Cooperative Agreement G12AC20038. The numerical simulations for this work were done on the supercomputing cluster in the Caltech Division for Geology and Planetary Science. The data supporting the analysis and conclusions is given in Figures and Tables. Data is accessible through the CaltechDATA repository (https://data.caltech.edu/records/1377). We thank Jean-Philippe Avouac, Victor Tsai, and Zhongwen Zhan for helpful discussions, Semechah Lui and Natalie Higgins for help with the simulation code, and Alice-Agnes Gabriel and an anonymous reviewer for thoughtful reviews that helped us improve the manuscript.

References

Abercrombie, R. E., & Rice, J. R. (2005). Can observations of earthquake scaling constrain slip weakening? *Geophysical Journal International*, *162*(2), 406–424. https://doi.org/10.1111/j.1365-246X.2005.02579.x

Allmann, B. P., & Shearer, P. M. (2009). Global variations of stress drop for moderate to large earthquakes. *Journal of Geophysical Research*, *114*, B01310. https://doi.org/10.1029/2008JB005821

Ampuero, J.-P., & Rubin, A. M. (2008). Earthquake nucleation on rate and state faults aging and slip laws. *Journal of Geophysical Research*, *113*, B01302. https://doi.org/10.1029/2007JB005082

Andrews, D. J. (2002). A fault constitutive relation accounting for thermal pressurization of pore fluid. *Journal of Geophysical Research*, *107*(B12), 2363. https://doi.org/10.1029/2002JB001942

Andrews, D. J. (2005). Rupture dynamics with energy loss outside the slip zone. *Journal of Geophysical Research*, *110*, B01307. https://doi.org/10.1029/2004JB003191

Baltay, A., Ide, S., Prieto, G., & Beroza, G. (2011). Variability in earthquake stress drop and apparent stress. *Geophysical Research Letters*, *38*, L06303. https://doi.org/10.1029/2011GL046698

Barbot, S., Lapusta, N., & Avouac, J.-P. (2012). Under the hood of the earthquake machine: Toward predictive modeling of the seismic cycle. *Science*, *336*(6082), 707–710. https://doi.org/10.1126/science.1218796

Brodsky, E. E., & Kanamori, H. (2001). Elastohydrodynamic lubrication of faults. *Journal of Geophysical Research*, *106*(B8), 16,357–16,374. https://doi.org/10.1029/2001JB000430

Brune, J. N. (1970). Tectonic stress and the spectra of seismic shear waves from earthquakes. *Journal of Geophysical Research*, *75*(26), 4997–5009. https://doi.org/10.1029/JB075i026p04997

Brune, J. N., Henyey, T. L., & Roy, R. F. (1969). Heat flow, stress, and rate of slip along the San Andreas fault, California. *Journal of Geophysical Research*, *74*(15), 3821–3827. https://doi.org/10.1029/JB074i015p03821

Chen, T., & Lapusta, N. (2009). Scaling of small repeating earthquakes explained by interaction of seismic and aseismic slip in a rate and state fault model. *Journal of Geophysical Research*, *114*, B01311. https://doi.org/10.1029/2008JB005749

Cocco, M., & Bizzarri, A. (2002). On the slip-weakening behavior of rate- and state dependent constitutive laws. *Geophysical Research Letters*, *29*(11), 1516. https://doi.org/10.1029/2001GL013999

Cocco, M., Bizzarri, A., & Tinti, E. (2004). Physical interpretation of the breakdown process using a rate- and state-dependent friction law. *Tectonophysics*, *378*, 241–262. https://doi.org/10.1016/j.tecto.2003.09.015

Cocco, M., Tinti, E., & Cirella, A. (2016). On the scale dependence of earthquake stress drop. *Journal of Seismology*, *20*, 1151–1170. https://doi.org/10.1007/s10950-016-9594-4

Di Toro, G., Goldsby, D. L., & Tullis, T. E. (2004). Friction falls towards zero in quartz rock as slip velocity approaches seismic rates. *Nature*, *427*(6973), 436–439. https://doi.org/10.1038/nature02249

Di Toro, G., Han, R., Hirose, T., De Paola, N., Nielsen, S., Mizoguchi, K., et al. (2011). Fault lubrication during earthquakes. *Nature*, *471*, 494.

Dieterich, J. H. (1979). Modeling of rock friction: 1. Experimental results and constitutive equations. *Journal of Geophysical Research*, *84*(B5), 2161–2168. https://doi.org/10.1029/JB084iB05p02161

Dieterich, J. H. (1994). A constitutive law for rate of earthquake production and its application to earthquake clustering. *Journal of Geophysical Research*, *99*(B2), 2601–2618. https://doi.org/10.1029/93JB02581

Dieterich, J. H. (2015). Applications of rate- and state-dependent friction to models of fault-slip and earthquake occurrence, (2nd ed.)., *Treatise on geophysics* (pp. 93–110). Netherlands: Elsevier. https://doi.org/10.1016/B978-0-444-53802-4.00075-0

Dieterich, J. H., & Smith, D. E. (2009). Nonplanar faults: Mechanics of slip and off-fault damage. *Pure and Applied Geophysics*, *166*, 1799–1815.

Dunham, E. M., Belanger, D., Cong, L., & Kozdon, J. E. (2011). Earthquake ruptures with strongly rate-weakening friction and off-fault plasticity, Part 2: Nonplanar faults. *The Bulletin of the Seismological Society of America*, *101*, 2308–2322. https://doi.org/10.1785/0120100076

Goldsby, D. L., & Tullis, T. E. (2002). Low frictional strength of quartz rocks at subseismic slip rates. *Geophysical Research Letters*, *29*(17), 1844. https://doi.org/10.1029/2002GL015240

Goldsby, D. L., & Tullis, T. E. (2011). Flash heating leads to low frictional strength of crustal rocks at earthquake slip rates. *Science*, *334*(6053), 216–218. https://doi.org/10.1126/science.1207902

Han, R., Shimamoto, T., Ando, J.-i., & Ree, J.-H. (2007). Seismic slip record in carbonate-bearing fault zones: An insight from high-velocity friction experiments on siderite gouge. *Geology*, *35*(12), 1131–1134. https://doi.org/10.1130/G24106A.1

Heaton, T. H. (1990). Evidence for and implications of self-healing pulses of slip in earthquake rupture. *Physics of the Earth and Planetary Interiors*, *64*(1), 1–20. https://doi.org/10.1016/0031-9201(90)90002-F

Hickman, S., & Zoback, M. (2004). Stress orientations and magnitudes in the SAFOD pilot hole. *Geophysical Research Letters*, *31*, L15S12. https://doi.org/10.1029/2004GL020043

Ida, Y. (1972). Cohesive force across the tip of a longitudinal-shear crack and Griffith's specific surface energy. *Journal of Geophysical Research*, *77*(20), 3796–3805. https://doi.org/10.1029/JB077i020p03796

Ide, S., & Beroza, G. C. (2001). Does apparent stress vary with earthquake size? *Geophysical Research Letters*, *28*(17), 3349–3352. https://doi.org/10.1029/2001GL013106

Kanamori, H., & Anderson, D. L. (1975). Theoretical basis of some empirical relations in seismology. *Bulletin of the Seismological Society of America*, *65*(5), 1073–1095.

Kanamori, H., & Brodsky, E. E. (2004). The physics of earthquakes. *Reports on Progress in Physics*, *67*(8), 1429–1496. https://doi.org/10.1088/0034-4885/67/8/r03

Kanamori, H., & Heaton, T. H. (2013). Geocomplexity and the physics of earthquakes, *Microscopic and macroscopic physics of earthquakes* (pp. 147–163). Washington, DC: American Geophysical Union (AGU). https://doi.org/10.1029/GM120p0147

Kanamori, H., & Rivera, L. (2013). Energy partitioning during an earthquake, *Earthquakes: Radiated energy and the physics of faulting* (pp. 3–13). Washington, DC: American Geophysical Union (AGU). https://doi.org/10.1029/170GM03

Kaneko, Y., & Shearer, P. M. (2014). Seismic source spectra and estimated stress drop derived from cohesive-zone models of circular subshear rupture. *Geophysical Journal International*, *197*(2), 1002–1015. https://doi.org/10.1093/gji/ggu030

Kaneko, Y., & Shearer, P. M. (2015). Variability of seismic source spectra, estimated stress drop, and radiated energy, derived from cohesive-zone models of symmetrical and asymmetrical circular and elliptical ruptures. *Journal of Geophysical Research: Solid Earth*, *120*, 1053–1079. https://doi.org/10.1002/2014JB011642

Knopoff, L. (1958). Energy release in earthquakes. *Geophysical Journal of the Royal Astronomical Society*, *1*(1), 44–52. https://doi.org/10.1111/j.1365-246X.1958.tb00033.x

Kostrov, V. V. (1974). Seismic moment and energy of earthquakes and seismic flow of rock. *Izvestiya, Academy of Sciences, USSR. Physics of the Solid Earth*, *1*, 23–44.

Lachenbruch, A. H., & Sass, J. H. (1980). Heat flow and energetics of the San Andreas fault zone. *Journal of Geophysical Research*, *85*(B11), 6185–6222. https://doi.org/10.1029/JB085iB11p06185

Lapusta, N., & Liu, Y. (2009). Three-dimensional boundary integral modeling of spontaneous earthquake sequences and aseismic slip. *Journal of Geophysical Research*, *114*, B09303. https://doi.org/10.1029/2008JB005934

Lapusta, N., Rice, J. R., Ben-Zion, Y., & Zheng, G. (2000). Elastodynamic analysis for slow tectonic loading with spontaneous rupture episodes on faults with rate- and state-dependent friction. *Journal of Geophysical Research*, *105*(B10), 23,765–23,789. https://doi.org/10.1029/2000JB900250

Lin, Y.-Y., & Lapusta, N. (2018). Microseismicity simulated on asperity-like fault patches: On scaling of seismic moment with duration and seismological estimates of stress drops. *Geophysical Research Letters*, *45*, 8145–8155. https://doi.org/10.1029/2018GL078650

Madariaga, R. (1976). Dynamics of an expanding circular fault. *Bulletin of the Seismological Society of America*, *66*(3), 639–666.

Madariaga, R. (1979). On the relation between seismic moment and stress drop in the presence of stress and strength heterogeneity. *Journal of Geophysical Research*, *84*(B5), 2243–2250. https://doi.org/10.1029/JB084iB05p02243

McGuire, J. J., & Kaneko, Y. (2018). Directly estimating earthquake rupture area using second moments to reduce the uncertainty in stress drop. *Geophysical Journal International*, *214*, 2224–2235. https://doi.org/10.1093/gji/ggy201

Noda, H., Dunham, E. M., & Rice, J. R. (2009). Earthquake ruptures with thermal weakening and the operation of major faults at low overall stress levels. *Journal of Geophysical Research*, *114*, B07302. https://doi.org/10.1029/2008JB006143

Noda, H., & Lapusta, N. (2010). Three-dimensional earthquake sequence simulations with evolving temperature and pore pressure due to shear heating: Effect of heterogeneous hydraulic diffusivity. *Journal of Geophysical Research*, *115*, B12314. https://doi.org/10.1029/2010JB007780

Noda, H., & Lapusta, N. (2012). On averaging interface response during dynamic rupture and energy partitioning diagrams for earthquakes. *Journal of Applied Mechanics*, *79*(3), 31,012–31,026.

Noda, H., Lapusta, N., & Kanamori, H. (2013). Comparison of average stress drop measures for ruptures with heterogeneous stress change and implications for earthquake physics. *Geophysical Journal International*, *193*(3), 1691–1712. https://doi.org/10.1093/gji/ggt074

Palmer, A. C., Rice, J. R., & Hill, R. (1973). The growth of slip surfaces in the progressive failure of over-consolidated clay. *Proceedings of the Royal Society of London. A. Mathematical and Physical Sciences*, *332*(1591), 527–548. https://doi.org/10.1098/rspa.1973.0040

Passelégue, F. X., Goldsby, D. L., & Fabbri, O. (2014). The influence of ambient fault temperature on flash-heating phenomena. *Geophysical Research Letters*, *41*, 828–835. https://doi.org/10.1002/2013GL058374

Poliakov, A. N. B., Dmowska, R., & Rice, J. R. (2002). Dynamic shear rupture interactions with fault bends and off-axis secondary faulting. *Journal of Geophysical Research*, *107*(B11), 2295. https://doi.org/10.1029/2001JB000572

Rempel, A. W., & Rice, J. R. (2006). Thermal pressurization and onset of melting in fault zones. *Journal of Geophysical Research*, *111*, B09314. https://doi.org/10.1029/2006JB004314

Rice, J. R. (1980). The mechanics of earthquake rupture. In A. M. Dziewonski & E. Boschi (Eds.), *Physics of the Earth's Interior* (pp. 555–649). Proc. International School of Physics Enrico Fermi, Course 78, 1979. Amsterdam, Netherlands: Italian Physical Society and North-Holland Publ. Co.

Rice, J. R. (1999). Flash heating at asperity contacts and rate-dependent friction. *Eos, Transactions American Geophysical Union*, *80*(46), F471.

Rice, J. R. (2000). Fracture energy of earthquakes and slip-weakening rupture parameters. *Eos, Transactions American Geophysical Union Fall Meeting Supplement*, *81*(48), F1227.

Rice, J. R. (2006). Heating and weakening of faults during earthquake slip. *Journal of Geophysical Research*, *111*, B05311. https://doi.org/10.1029/2005JB004006

Rice, J. R., & Andy, R. (1983). Stability of steady frictional slipping. *Journal of Applied Mechanics*, *50*(2), 343–349.

Rice, J. R., Lapusta, N., & Ranjith, K. (2001). Rate and state dependent friction and the stability of sliding between elastically deformable solids. *Journal of the Mechanics and Physics of Solids*, *49*(9), 1865–1898. The JW Hutchinson and JR Rice 60th Anniversary Issue https://doi.org/10.1016/S0022-5096(01)89400042-4

Rice, J. R., & Ruina, A. (1983). Stability of steady frictional slipping. *Journal of Applied Mechanics*, *50*(2), 343–349.

Rubin, A. M., & Ampuero, J.-P. (2005). Earthquake nucleation on (aging) rate and state faults. *Journal of Geophysical Research*, *110*, B11312. https://doi.org/10.1029/2005JB003686

Ruina, A. (1983). Slip instability and state variable friction laws. *Journal of Geophysical Research*, *88*(B12), 10,359–10,370. https://doi.org/10.1029/JB088iB12p10359

Sibson, R. H. (1973). Interactions between temperature and pore-fluid pressure during earthquake faulting and a mechanism for partial or total stress relief. *Nature Physical Science*, *243*(126), 66–68. https://doi.org/10.1038/physci243066a0

Sibson, R. H. (1975). Generation of pseudotachylyte by ancient seismic faulting. *Geophysical Journal of the Royal Astronomical Society*, *43*(3), 775–794. https://doi.org/10.1111/j.1365-246X.1975.tb06195.x

Sulem, J., & Famin, V. (2009). Thermal decomposition of carbonates in fault zones: Slip-weakening and temperature-limiting effects. *Journal of Geophysical Research*, *114*, B03309. https://doi.org/10.1029/2008JB006004

Viesca, R. C., & Garagash, D. I. (2015). Ubiquitous weakening of faults due to thermal pressurization. *Nature Geoscience*, *8*(11), 875–879. https://doi.org/10.1038/ngeo2554

Wibberley, C. A. J., & Shimamoto, T. (2005). Earthquake slip weakening and asperities explained by thermal pressurization. *Nature*, *436*(7051), 689–692. https://doi.org/10.1038/nature03901

Williams, C. F., Grubb, F. V., & Galanis Jr., S. P. (2004). Heat flow in the SAFOD pilot hole and implications for the strength of the San Andreas fault. *Geophysical Research Letters*, *31*, L15S14. https://doi.org/10.1029/2003GL019352

Ye, L., Lay, T., Kanamori, H., & Rivera, L. (2016). Rupture characteristics of major and great ($M_w \geq 7.0$) megathrust earthquakes from 1990 to 2015: 1. Source parameter scaling relationships. *Journal of Geophysical Research: Solid Earth*, *121*, 826–844. https://doi.org/10.1002/2015JB012426

Zoback, M. D., Zoback, M. L., Mount, V. S., Suppe, J., Eaton, J. P., Healy, J. H., et al. (1987). New evidence on the state of stress of the San Andreas fault system. *Science*, *238*(4830), 1105–1111. https://doi.org/10.1126/science.238.4830.1105

Erratum

Due to a typesetting error, image files for Figures 14 and 15, illustrating the maximum fault temperature changes and static stress drops for models with varying VS properties, respectively, were interchanged in the originally published version of this manuscript. The error has been corrected, and this may be considered the official version of record.